
Characterizing the variability of natural gas hydrate composition from a selected site of the Western Black Sea, off Romania

Chazallon B. ^{1,*}, Rodriguez C.T. ¹, Ruffine Livio ², Carpentier Y. ¹, Donval Jean-Pierre ², Ker Stephan ², Riboulot Vincent ²

¹ Univ. Lille, CNRS, UMR 8523, PhLAM – Physique des Lasers, Atomes et Molécules, CERLA – Centre d'Etudes et de Recherche Lasers et Applications, F-59000, Lille, France

² IFREMER, Département Ressources physiques et Ecosystèmes de fond de Mer (REM), Unité des Géosciences Marines, 29280, Plouzané, France

* Corresponding author : B. Chazallon, email address : Bertrand.Chazallon@univ-lille.fr

Abstract :

Natural Gas Hydrates (NGH) collected during the Ghass cruise 2015 in the Western Black Sea onboard the R/V Pourquoi pas? are characterized by a suite of techniques. Gas Chromatography and Raman spectroscopy are used for the identification of the nature of the gas source, the hydrate structure and spatial variability of cage occupancies. The nature and source of hydrate forming gases primarily reveal a high methane content (99.6 mol%) and small amount of nitrogen (>0.29 mol%) and CO₂ (0.056 mol%). Isotopic analyses from the hydrate-bound methane and recently published results from Pape et al. (2020) clearly indicate a microbial source of gas supplying the hydrate deposit generated by the reduction of carbon. For the first time, Micro-Raman imaging spectroscopy was applied to the Western Black Sea NGH and the results show a heterogeneous distribution of the encapsulated guest molecules (CH₄, N₂ and H₂S), which is associated with a spatial variability of the guest-gas composition at the micron-scale. Some portions of the 2D-Raman images clearly exhibit a relative N₂-enrichment (with a concentration exceeding 6 mol% N₂ at some positions), while H₂S shows a rather minor contribution on all the spectral maps investigated. A correlation is then established between the composition of the gas in the NGH and its impact on the CH₄ cage occupancy, with a ratio of θ_{LC}/θ_{SC} (large cage/small cage) between ~ 0.5 and 1.26 depending on the positions analyzed. The departure from the expected ratio in pure methane hydrate is attributed to the preferential encasement of N₂ in the large cage of the NGH structure. In addition, the occurrence of carotenoids identified in sediment-rich zones show a minor impact on the CH₄ cage occupancies. The results are discussed within the context of natural gas resource estimates in NGH to emphasize how the measured cage occupancies may impact the volumetric conversion factor commonly used with other geologic parameters to determine the resource endowment and global volume of methane. The small-scale heterogeneities revealed by the 2D-Raman images point out the importance to better understand stages of hydrates formation in methane-rich seafloor environment.

Highlights

► NGH from Black Sea are investigated by gas chromatography and Raman spectroscopy. ► The hydrates are structure I and contain mainly CH₄ and small amounts of N₂ and CO₂. ► CH₄ being generated by the reduction of CO₂. ► 2D-Raman reveals spatial variability in guests' distribution and hydrate composition. ► Raman imaging analysis shows a spatial variability of the cage occupancy.

Keywords : Natural gas hydrates, Black sea, Methane, Cage occupancy

1 **1. Introduction**

2 Natural gas hydrates (NGH) are ice-like crystalline compounds in which hydrogen-
3 bonded water molecules form specific cages able to encase low molecular weight molecules.
4 They are usually stable at low temperature and high pressure. The water framework is called
5 the “host” and the inserted molecule, the “guest”. Previous studies have shown that gas
6 hydrates (GH) are non-stoichiometric compounds in which not all the cages need to be filled
7 with a gas molecule to stabilize the whole structure (Sloan and Koh, 2008). Depending on the
8 physico-chemical properties of the guest molecule, three main crystallographic structures can
9 be found in nature (Bourry et al., 2007, 2009; Chazallon et al., 2007; Khlystov et al., 2013;
10 Kida et al., 2006; Lu et al., 2007): cubic structure I (sI) (lattice parameter $a \sim 12 \text{ \AA}$, cubic
11 structure II (sII) (lattice parameter $a \sim 17 \text{ \AA}$) and hexagonal structure H (sH) (lattice parameter
12 $a \sim 12 \text{ \AA}$ and $c \sim 10 \text{ \AA}$). NGH are mainly composed of microbial methane, and thus sI is the
13 most encountered structure in nature (Lu et al., 2007; Makogon et al., 2007), whereas
14 structures sII (Bourry et al., 2009; Brooks et al., 1984; Davidson et al., 1986a; Pape et al.,
15 2010) and sH (Lu et al., 2007; Yousuf et al., 2004) are less common, and require sources of
16 thermogenic gases containing non-methane hydrocarbons to stabilize the structure.

17 NGH represent one of the largest methane reservoir on Earth with the total amount of
18 carbon stored higher than all conventional hydrocarbon reserves (Lu, 2015; Ruppel and
19 Kessler, 2017; Wallmann et al., 2012). Furthermore, it has been estimated that ~98-99 % of
20 NGH are sequestered within marine sediments in the first tens to hundreds of meters of
21 sediment on continental margins (Boswell et al., 2020; Kvenvolden, 1988), while other
22 occurrences concern the permafrost region (Paull and Dillon, 2000). The current substantial
23 efforts in NGH research to better characterize these deposits (Ruffine et al., 2018; Song et al.,
24 2014) is justified by the fact that marine methane hydrates are nowadays viewed as a double-
25 edged sword. On the one hand, a large proportion of the enclathrated methane might be
26 produced in the future to meet the increasing world energy demand, and on the other hand, the
27 temperature-sensitive hydrate deposits can be destabilized due to ocean warming. This would
28 lead to the release of methane into the water column with potential input into the atmosphere
29 as well as potential destabilization of the seafloor, hastening and perpetuating the cycle of
30 global warming (Kennett et al., 2003; Maslin et al., 2010; Ruppel and Kessler, 2017).
31 Accordingly, NGH may be an opportunity or a threat for modern societies (Wang et al.,
32 2018).

1 Elements of response for these two social issues may be obtained through the
2 evaluation of the methane quantities stored in NGH deposits, and this requires in-depth micro-
3 scale characterization of guest identification and distribution in hydrates. Up to now, most
4 global estimates of gas trapped in NGH have often been calculated assuming (based on
5 structure sI) a mean cage occupancy of 85%, i.e., a hydration number n of methane hydrate of
6 ~ 6.75 which corresponds to a volumetric conversion factor of $\sim 164 \text{ m}^3$ of methane per m^3 of
7 hydrate (Boswell and Collett, 2011; Kvenvolden, 1998). Actually, it turns out that both the
8 cage occupancies (θ_{LC} and θ_{SC} being the large and small cage occupancies, respectively) and
9 hydration numbers are key parameters to evaluate the volumetric conversion factor. These
10 parameters (θ_{LC} , θ_{SC} , n) can reliably be determined by spectroscopic technics (Raman or
11 NMR-Nuclear Magnetic Resonance) (Chazallon et al., 2007; Liu et al., 2015; Lu et al., 2005;
12 Ripmeester et al., 2005; Uchida et al., 1999). However, it has been shown that methane cage
13 occupancy can vary significantly in NGH with a ratio of $\theta_{\text{LC}}/\theta_{\text{SC}} \sim 0.86\text{-}1.51$, depending on
14 the area where they are collected. Even for NGH deposits for which methane is
15 overwhelmingly present, a ratio of $\theta_{\text{LC}}/\theta_{\text{SC}}$ lower than 1 has already been observed (H. Lu et
16 al., 2011b; Z. Lu et al., 2011; Ripmeester et al., 2005). Similarly, a variability of the cage
17 occupancy ratio ($\theta_{\text{LC}}/\theta_{\text{SC}}$ between ~ 2.38 and ~ 1.18) in NGH containing nearly pure methane
18 was reported (Yeon et al., 2011). It was suggested that such abnormal methane occupancy
19 (i.e., corresponding to a deviation from that usually found in synthetic pure CH_4 -hydrate) in
20 NGH embedded in clay-rich deep-sea-sediments could be due to mobile ions (sodium cations)
21 present in the clay interlayers (Seo et al., 2009; Yeon et al., 2009). These latter could
22 significantly affect the NGH stability, impact the CH_4 cage occupancy and the hydration
23 number and thus the estimates of the quantity of gas trapped.

24 In the present study, we combined two different techniques (gas chromatography and
25 micro-Raman spectroscopic imaging) to characterize samples of natural hydrates collected
26 during the Ghass cruise (2015) in the Romanian water sector of the Western Black Sea, which
27 is known as the largest anoxic and methane-rich water mass on Earth. The Black sea contains
28 several identified and inferred NGH deposits along its margin (Colin et al., 2020; Haeckel et
29 al., 2015; Heeschen et al., 2011; Minshull et al., 2020; Nasif et al., 2020; Pape et al., 2011;
30 Popescu et al., 2007; Zander et al., 2020). Our molecular-scale approach allowed to
31 investigate the variability in cage occupancy and the impact of the presence of minor guest
32 components on the overall methane content.

33

2. Geological setting and sampling

The study area in the Black Sea is characterized by a large number of widespread gas seeps, (Egorov et al., 2011; Naudts et al., 2006; Schmale et al., 2005, 2011) with a clear link between the pattern of seep distribution and the gas hydrate stability zone (GHSZ) (Riboulot et al., 2017). Indeed, the gas flares detected in the water column from ship-borne multi-beam echo-sounding are primarily located on the shelf and outside the area delimited by GHSZ, suggesting that the hydrate deposits act as a barrier preventing intense methane release at locations where hydrates are stable (Fig. 1).

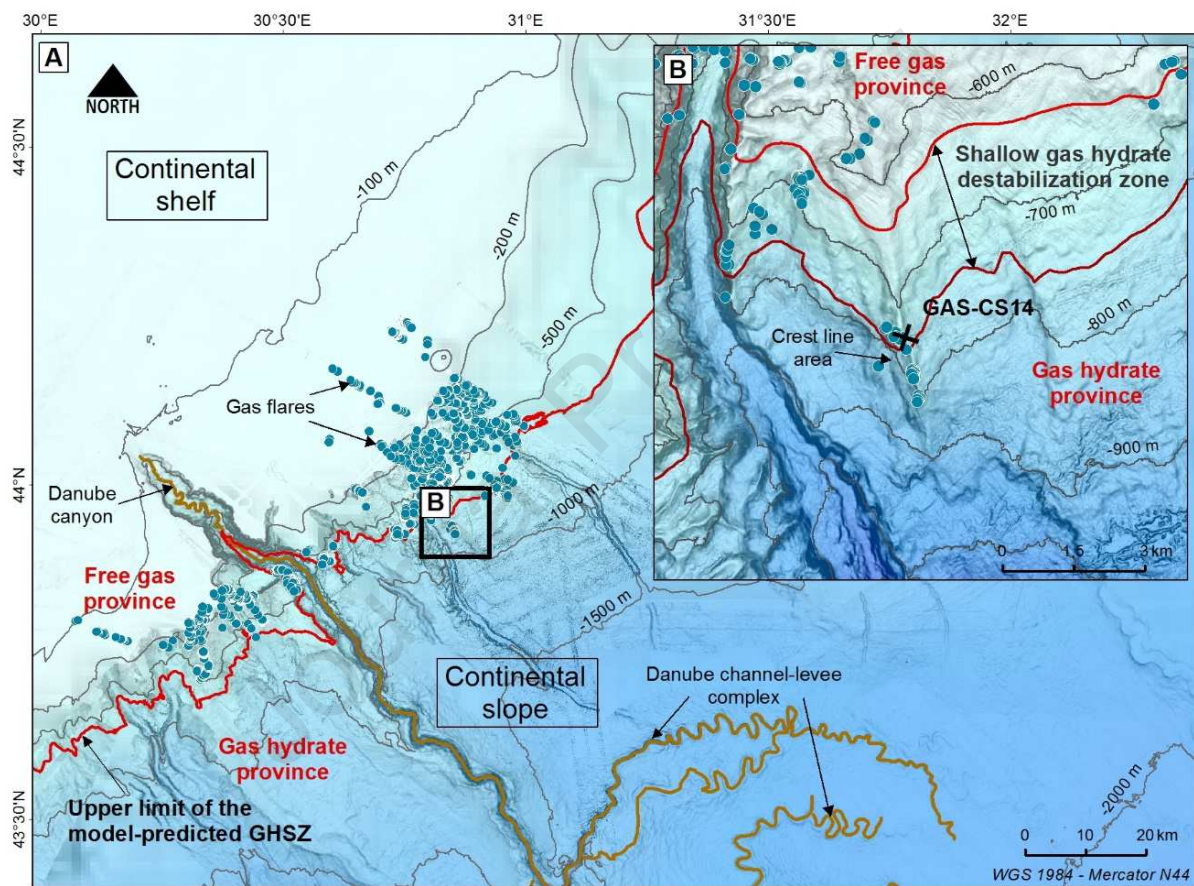


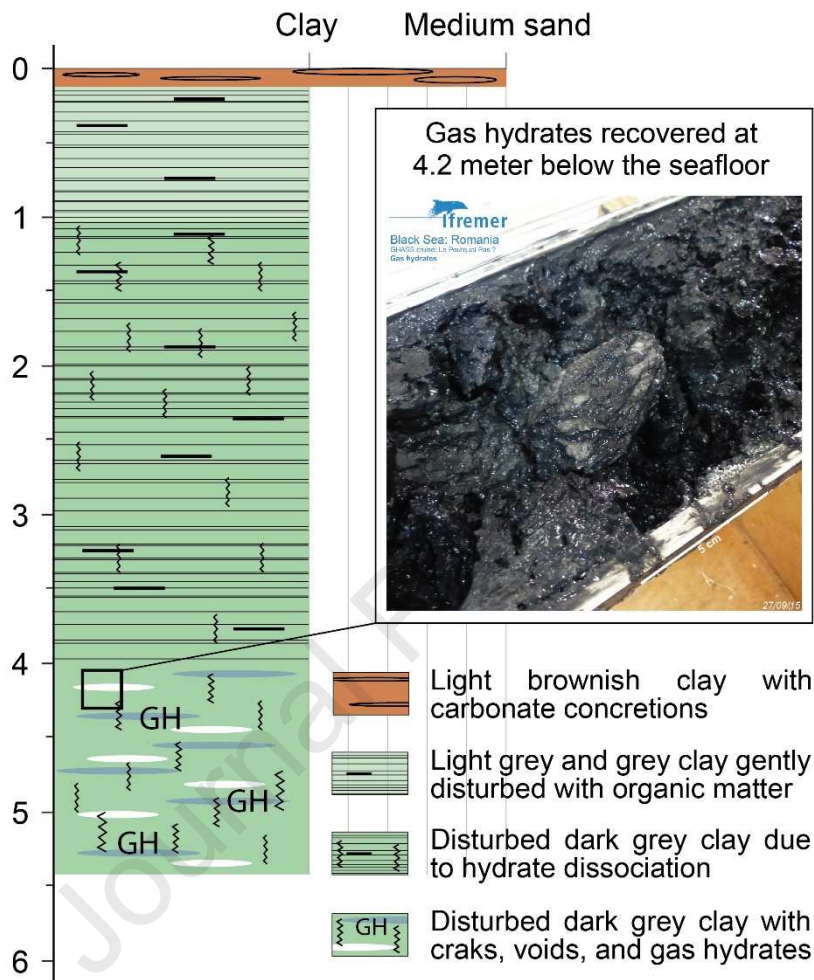
Fig. 1: A Bathymetric map of the Romanian sector of the Black Sea showing the Danube canyon and the location of the study area on the continental slope inside the gas hydrate province. The upper limit of the predicted base of the Gas Hydrate Stability Zone (GHSZ) is indicated by the thick red line (Ker et al., 2019). The blue dots highlight the acoustic gas flares identified in the water column during the GHASS cruise (Riboulot et al., 2017). They are mostly located above the GHSZ but can also be found at the landward termination of the GHSZ and within the GHSZ in the Crest line area. B. Close-up view of the study area with location of the Calypso core GAS-CS14 recovered at the summit of the crest line close to gas flares. This core, where the gas hydrates were sampled, is located at the limit of the shallow gas hydrate stability zone identified previously (Riboulot et al., 2018). This corresponds to the boundary area where gas hydrates are undergoing destabilization due to seawater infiltration within the sediment since the Black Sea reconnection with the Mediterranean Sea, leading to the increase of salinization of the pore water.

1 Riboulot et al. (2018) and Ker et al. (2019) calculated the boundary of the GHSZ between 660
2 and 720 m (Fig. 1), as proposed previously for seeps in the Dnepr paleo-delta area in the NW
3 Black Sea (Naudts et al., 2006). A large number of seeps were detected around this water
4 depth range, and Riboulot et al. (2018) suggest that the occurrence of these gas seeps is
5 related to the dissociation of hydrates due to the ongoing salt intrusion from today's Black
6 Sea marine bottom waters into the lacustrine sediment since the reconnection with the
7 Mediterranean Sea about 9000 years ago (Soulet et al., 2011). While seeps' density was much
8 less pronounced inside the GHSZ, seeps were found only at specific locations where faults
9 reach the seafloor along a crest line area (Ker et al., 2019). The hydrates were collected from
10 coring operations on this crest line (Fig. 1), where several persistent and focused gas flares
11 were detected from the shipborne echo-sounder during the Ghass cruise. Thus, this site is
12 classified as being a high-flux fluid system. The hydrate-bearing core, GAS-CS14
13 (N43°56.361'; E30°51.044'), was retrieved using a long Calypso piston corer at 738 m water
14 depth. It was the unique core containing hydrates from a series of >20 cores, and it was
15 mainly composed of Unit 3 lacustrine sediment (Ross and Degens, 1974). The youngest
16 sediments deposited during the Holocene, representing the lacustrine-marine transition (Unit
17 II) and the marine stage (Unit I), were not clearly identifiable; possibly due to a loss of the
18 uppermost part of the core as explained by Ruffine et al. (2021). Thus, hydrates were located
19 within the lacustrine sediments. This is in agreement with Pape et al. (2010) who found a
20 higher concentration of hydrates in Unit III from cores collected off Georgia.

21

Core: **GAS-CS014**
 Length: 5.42 m
 Water depth: 738 m

Lithofacies



1

2 **Fig. 2:** Description of the hydrate-bearing core with localization of the hydrate zone within the sample.

3

4 The hydrate-bearing sediment samples were collected in the core GAS-CS14 at ~738 m water
 5 depth and ~9 °C, which corresponds to the Black Sea bottom water temperature (see Fig. 2 for
 6 further details on the description of the core and location of hydrate samples). Core GAS-
 7 CS14 has a length of 542 cm, and was subdivided in four lithofacies as described in Fig. 2. Its
 8 topmost part highlights 10 cm of light brownish clay with numerous small carbonate
 9 concretions. This carbonate-contained section is followed by a sedimentary sequence
 10 dominated by grey clay that turns to sediment dark and reworked, and such darkness and
 11 reworking become more pronounced with increasing depth. The sediment is highly
 12 unstructured and reworked within the hydrate-bearing interval as shown in the photo of Fig. 2.

1 X-ray diffraction applied to the sediment in another study (Ruffine et al., 2021) reveals that
2 clays and mica represent between 53 and 67 wt.% of the matrix, with illite being by far the
3 dominant species. The remaining minerals are mainly silicates (feldspar, plagioclase and
4 quartz) and carbonates. A thin layer of few centimeters of light brownish clay with small
5 carbonate concretions was identified at the uppermost part of the core followed by a light grey
6 clay containing organic matter, whereas the hydrate-bearing zone consists of dark grey clay.
7 Evidence of core disturbances increases when moving towards the hydrate bearing-zone (Fig.
8 2). Sulfate concentration was < 1 mM within the first decimeter of sediment (Ruffine et al.,
9 2021).

10
11

12 **3. Experimental methods**

13 After recovery, the hydrate-bearing core were brought to the ship laboratory and split
14 lengthwise. The core consists of centimeter scale hydrate nodules and lens. Small hydrate
15 samples were immediately prepared for gas analysis, and the remaining hydrates stored into
16 liquid nitrogen as quickly as possible, without determining their depth location. However, for
17 the molecular and isotopic ($\delta^{13}\text{C}$ and δD) composition analyses of the hydrate-bound gases,
18 the samples were taken from the first hydrate-bearing core section identified visually, thus
19 they were located within the 4-5 m depth interval. Hydrate nodule samples of more than 5 cm
20 size were taken (Fig. 2) and cleaned of sediment, and placed in 10 mL glass vials which were
21 then air vacuumed. The coexistence of free gas trapped during hydrate formation cannot
22 firmly be excluded. However, such remaining pore gas will be a minor fraction of the gases
23 collected from the hydrate-sample dissociation. Therefore, we believe that the collected
24 samples are representative of the hydrate-bound gases. Two different hydrate samples were
25 analyzed. Molecular composition analysis was performed at the Laboratoire des Cycles
26 Géochimiques et ressources (LCG) of Ifremer using a gas chromatograph $\mu\text{GC R3000}$ from
27 SRA equipped with a $\mu\text{Thermal Conductivity Detector}$ and a 8m, 0.32 mm PoraPlot U
28 capillary column to quantify both methane and carbon-dioxide. The concentrations of heavier
29 hydrocarbons, from ethane to n-hexane, were measured on a gas chromatograph Agilent
30 7890A equipped with a 32 m, 0.32 mm x 30 μm Porapak Q column. The configuration of the
31 chromatograph is not suitable for hydrogen sulfide. The instrument was calibrated against
32 standard gas mixtures, and both the relative accuracy and standard deviation were of $\pm 2\%$ for
33 methane and carbon dioxide concentrations, and $\pm 4\%$ for the heavier hydrocarbons.

1
2 Isotopic analyses were performed on two hydrate samples at Isolab B.V. (Neerijnen, The
3 Netherlands) for methane, ethane, propane and carbon dioxide using gas chromatograph-
4 isotope ratio-mass spectrometers (GC-IR-MS). Labco® vials of 12 mL were filled with the
5 hydrate-bound gases at ~0.2 MPa. Carbon ($\delta^{13}\text{C}$) and hydrogen (δD) stable isotope ratios
6 were measured when appropriate. An Agilent 6890N gas chromatograph interfaced to a
7 Finigan Delta S IRMS and a Finigan GC-C II interface (Thermo) was used for the analysis of
8 the stable carbon isotopes of methane. The GC is equipped with a 12m, 0.32mm molsieve
9 column (Agilent) and an injection valve. Stable carbon isotopes of heavier hydrocarbons and
10 carbon dioxide were measured on an Agilent 7890A gas chromatograph interfaced with a
11 MAT 253 IRMS using a GC-Isolink or a Finigan GC-C III interface. The GC is equipped with
12 a 25m, 0.32mm Porabond-Q column (Agilent) and an injection valve. δD measurement was
13 carried out on an Agilent 7890A gas chromatograph equipped with a 25m, 0.32mm molsieve
14 column (Agilent) and an injection valve, and interfaced with a MAT 253 IRMS and using a
15 GC-Isolink interface from Thermo. For calibration purpose, the instruments were regularly
16 checked with a calibration standard. Results are as part per thousand (‰) relative to the
17 Vienna PeeDee Belemnite Standard (VPDB) and the Vienna Standard Mean Ocean Water
18 (VSMOW) for $\delta^{13}\text{C}$ and δD , respectively. The uncertainties in the $\delta^{13}\text{C}$ and δD measurements
19 were given as ± 0.1 - 0.3 ‰ and ± 2 ‰, respectively.

20 NGH recovered from core GAS-CS14 were further analyzed by optical microscopy and
21 Raman spectroscopy. Since the hydrates likely underwent partial decomposition during the
22 recovery onboard and before storage in liquid nitrogen at 77 K, focus was made on central
23 pieces from five hydrate subsamples (typically ~5 mm long) in a well-preserved state. For
24 that, a small part of the NGH was placed in a mortar filled with liquid nitrogen and it was
25 carefully crushed into smaller pieces. Each piece was placed in a cooling stage set at a
26 working temperature of 128 K, in an atmosphere saturated with nitrogen gas. A more detailed
27 description of our sample loading protocol and hydrate probing using Raman systems can be
28 found in (Bourry et al., 2009; Charlou et al., 2004; Chazallon et al., 2007, 2017). Note that we
29 exclude any sample degradation during the long-term storage of NGH samples in liquid
30 nitrogen because the NGH remains frozen. More specifically, nitrogen from the liquid does
31 not interfere with the composition of the sample due to the higher volatility of N_2 in
32 comparison with CH_4 , thus avoiding any exchange reaction with methane. Also, permeation
33 processes of N_2 in the sample can be excluded as these would be too slow to occur within the

1 time frame of this study (Salamatın et al., 2017). Raman measurements were performed at
2 PhLAM laboratory (Lille, France) using an InVia Reflex Raman spectroscope (Renishaw).
3 The spectral resolution was set to $\sim 4 \text{ cm}^{-1}$ with a holographic grating of 1800 grooves/mm
4 and a Peltier cooled front illuminated CCD detector. The excitation radiation ($\lambda = 514.5 \text{ nm}$)
5 was produced by a DPSS laser (Cobolt®). An Olympus free-space microscope was coupled to
6 the spectrometer and Raman spectra were collected through a 50× objective (0.5 N.A.) that
7 provides a circular beam spot smaller than $\sim 1.5 \text{ }\mu\text{m}$ diameter. The probed sample volume
8 depends on several factors related to the NGH refraction index and the properties of the
9 collection optics; it is estimated at several tens of μm^3 to $100 \text{ }\mu\text{m}^3$ for the most transparent
10 part of the sample. The laser power focused onto the sample was typically adjusted to 3-4
11 mW, as measured by a Lasercheck power-meter (Coherent). High signal-to-noise-ratios (S/N)
12 of individual spectra collected in this work were obtained with integration times of typically
13 60 s in one or two accumulations. A set of 48 Raman maps were collected in synchroscan
14 mode (section 4.3) and representative information was extracted from two of them (see
15 section 4.3 and supplementary material for further details). Errors in the measured integrated
16 intensity are estimated from the lowest values found for the different components. It gives for
17 CH_4 and H_2O a maximal relative error of respectively $\sim 2\%$ and 0.2% , whereas for N_2 and H_2S
18 the maximal relative error is estimated at $\sim 12\%$. The detection limit was estimated from the
19 standard deviation (σ_b) of the blank signal in a region free of Raman peaks. The minimal
20 (S/N) of CH_4 and H_2O were found at least two orders of magnitude higher than the adopted
21 criterion of $3 \times \sigma_b$. For the components present at lower concentrations, the minimal cut-off of
22 the contour lines of the Raman map of N_2 and H_2S was set to 75 in order to adopt a high
23 confidence level of detection for these species (see section 4.3). In addition, the errors on the
24 guest concentrations derived from error propagation were found between 0.1 mol% (for the
25 highest S/N ratio) and 1.7 mol% (for the lowest S/N ratio).

26

27 **4. Results and discussion**

28 *4.1 Nature and source of the hydrate-forming light hydrocarbons*

29 The analysis of the gases from the two decomposed hydrate samples indicates that they
30 primarily contain methane ($> 99.5 \text{ mol}\%$), followed by nitrogen ($> 0.29 \text{ mol}\%$) and carbon
31 dioxide ($> 0.041 \text{ mol}\%$). Their compositions are slightly different from one sample to another.
32 Ethane and propane are in trace amount (Table 1). Methane and ethane are highly depleted in
33 ^{13}C , with values around -70 and -63 ‰ , respectively, whereas the propane is more enriched in

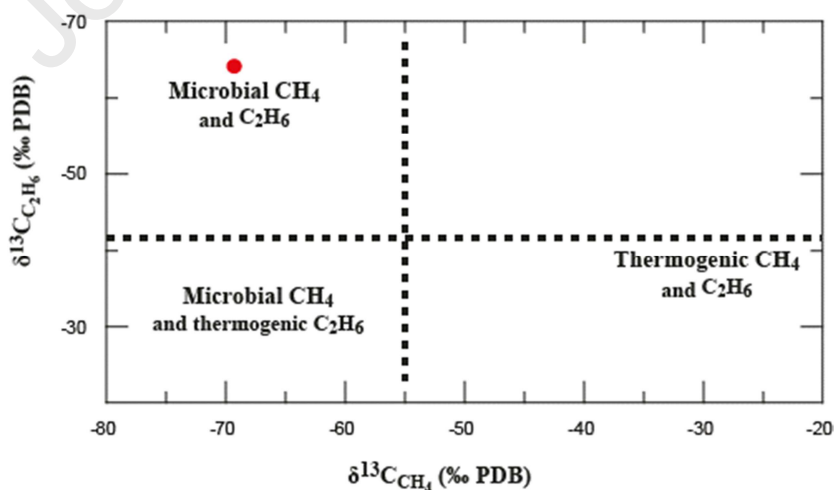
1 ^{13}C ($\delta^{13}\text{C}\text{-C}_3\text{H}_8$ around -27 ‰). Pape et al. (2020) analyzed void gases collected in sediments
 2 from deeper depths at the same study area, and they measured similar $\delta^{13}\text{C}$ values for
 3 methane. They also found that ethane and propane were slightly enriched in ^{13}C with values
 4 ranging between -55.7 and -23.2 ‰ and -23.2 and -19.8 ‰, respectively.

6 **Table 1:** Molecular and isotopic compositions of the hydrate-bound gases from two different samples.

		N_2	CH_4	CO_2	C_2H_6	C_3H_8	$\text{CH}_4/(\text{C}_2\text{H}_6 + \text{C}_3\text{H}_8)$
SAMPLE 1	mol. %	0,3796	99,5571	0,0560	0,0071	0,0002	13638
	$\delta^{13}\text{C}$ (‰)		-69.3	-22.3	-63.6	-27.8	
	δD (‰)		-291		-250		
SAMPLE 2	mol. %	0,2933	99,6570	0,0416	0,0078	0,0003	12303
	$\delta^{13}\text{C}$ (‰)		-69.4	-22.1	-63.6	-27.9	
	δD (‰)		-290		-250		

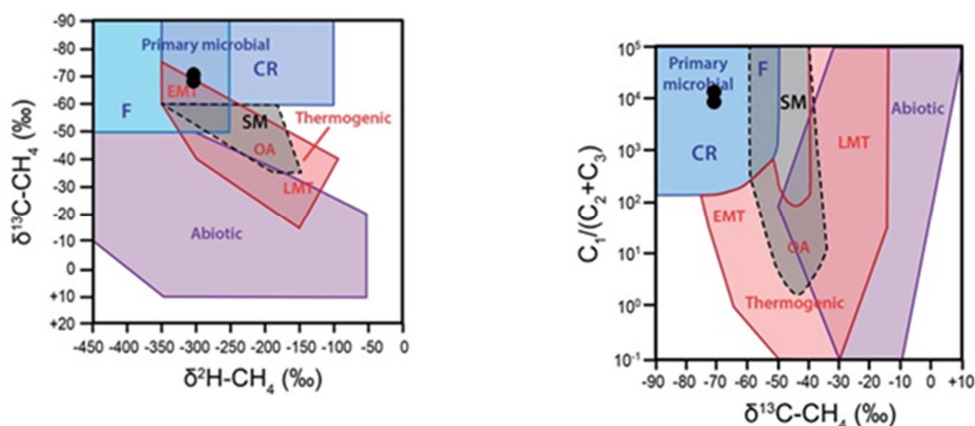
7
 8 Both molecular and isotopic compositions of the light hydrocarbons were measured to
 9 construct the classical geochemical diagrams used for source determination (Fig. 3). Fig. 3a
 10 clearly indicates a microbial source of methane and ethane supplying the hydrate deposit. The
 11 CD ($\delta^{13}\text{C}$ vs δD) diagram (Fig. 3b) shows that methane from both samples falls within an
 12 overlapping area indicating that either methyl fermentation (F) or carbon dioxide reduction
 13 (CR) can generate the methane trapped in the hydrates. However, Fig. 3c conclusively
 14 indicates that the hydrate-bound methane is generated from carbon dioxide reduction.

15 a)



b)

c)



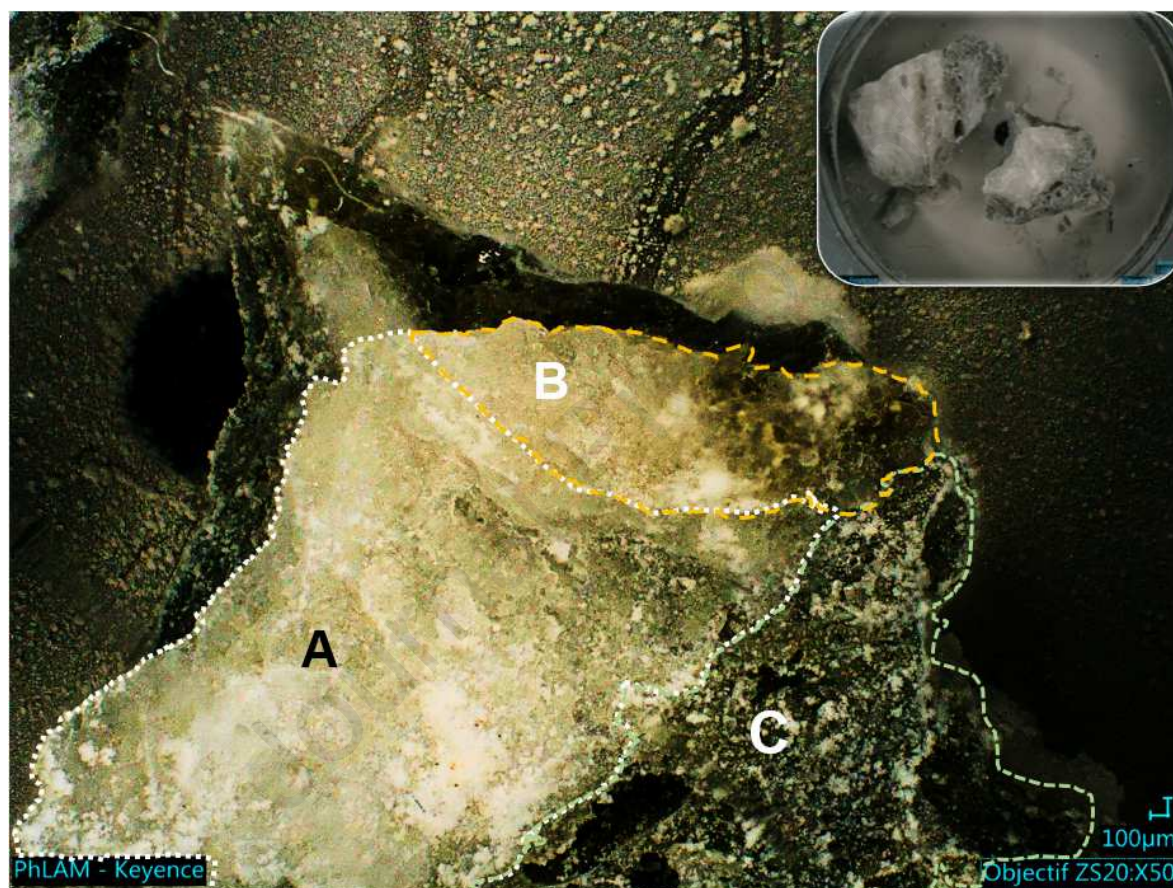
1 **Fig. 3:** Source assessment of the light hydrocarbons of the hydrate-bound gases from geochemical diagrams in
 2 the a) $\delta^{13}\text{C-CH}_4$ vs. $\delta^{13}\text{C-C}_2\text{H}_6$ space (modified after (Bernard et al., 1978) and (Milkov, 2011)), b) $\delta^2\text{H-CH}_4$ vs
 3 $\delta^{13}\text{C-CH}_4$ space (modified after (Bernard et al., 1978)), c) $\delta^{13}\text{C-CH}_4$ vs. $\text{CH}_4/(\text{C}_2\text{H}_6 + \text{C}_3\text{H}_8)$ space (modified after
 4 (Bernard et al., 1978) and (Milkov and Etiope, 2018))

5
 6 This is in agreement with previous studies that have shown that methane in the area of
 7 the Danube deep-sea fan of the Black Sea and off Crimea is sourced from carbonate reduction
 8 (Pape et al., 2020; Römer et al., 2012; Zander et al., 2020). Moreover, Pape et al. (2020) show
 9 that the relatively depleted $\delta\text{D-CH}_4$ observed for methane is inherited from the formation
 10 water generated during relatively cold periods of the Black Sea history. The origin of propane
 11 is unclear, and in the absence of clear evidence of thermogenic gases, one may be tempted to
 12 think that it is also generated from microbial processes. However, thermogenic gases were
 13 found in both the Eastern and Western Black Sea (Pape et al., 2010; Reitz et al., 2011;
 14 Rusakov and Kutas, 2018), and the trace of propane measured in the hydrate samples may
 15 also come from leaking thermogenic sources. Without information on the $\delta\text{D-propane}$ or the
 16 concentration measurement of hydrocarbons from butane to hexane, the origin of the propane
 17 remains elusive.

18 19 *4.2 Properties of the hydrate samples from optical microscopy and single-point* 20 *Raman analysis*

21
 22 Fig. 4a shows a high-resolution image (min: 1600 x 1200 pixels) obtained with a 3D-
 23 microscope (Keyence) of a representative view of a selected small part of the NGH. The
 24 sample is maintained intact at liquid nitrogen temperature. It can be divided into three major
 25 zones where the GH was shown to be present in different relative amount (see next section):
 26 1) a light-grey zone free of sediment, with white patches (A, Fig. 4, delineated by a white

1 dotted line) which corresponds to a GH-rich zone mixed with frozen water (ice phase) 2) a
 2 light-brown zone with dark patches (sediment) (B, Fig 4, delineated by an orange-dotted line)
 3 which is also a GH-rich zone where the brown color indicates the presence of iron-bearing
 4 minerals at an elevated concentration in the Black Sea (Egger et al., 2016), as also shown in a
 5 complementary study (Ruffine et al., 2021), 3) a dark-grey area with small white patches,
 6 which is a less rich GH-zone, at the bottom right-hand side (Fig. 4, C, delineated by a green
 7 dotted line) where solid hydrates (or ice) are intermixed with sediments.

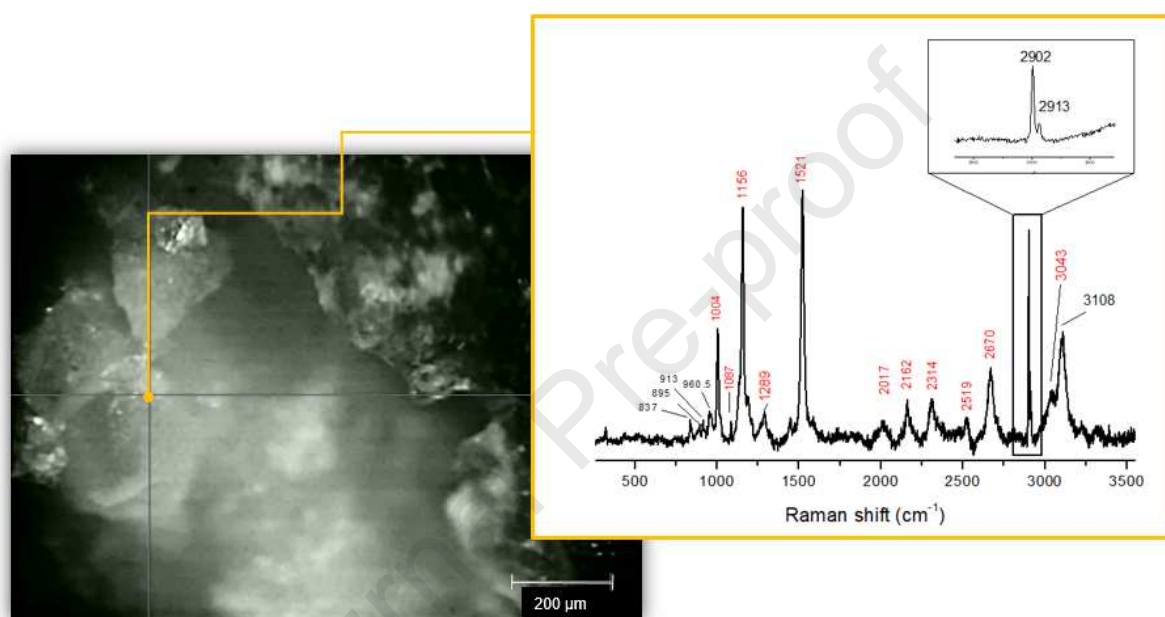


8 **Fig. 4:** 3D microscopic image (objective x20) of the NGH collected in the Black Sea. The light-grey zone with
 9 white patches (A, delineated by a white-dotted line) indicates the presence of bulk ice and/or hydrates, a light
 10 brown zone (B, delineated by an orange-dotted line) with small dark patches (right corner of the orange-dotted
 11 line) consistent with the presence of iron-bearing minerals (see text for details), a dark-grey area at the bottom
 12 right-hand side with small white patches (C, delineated by a light-green dotted line) indicating solid hydrates (or
 13 ice) intermixed with sediments. The inset (top right) shows a macroscopic view of hydrates pieces extracted
 14 from the core.

15 *4.2.a Raman signature of the sediment-rich zone*

16 Single-point Raman spectra of typically four to five randomly-chosen locations at the
 17 surface of a freshly cut part of the NGH were collected over the range of 100 cm^{-1} to 3800 cm^{-1}

1 ¹. They show the predominance of methane gas trapped in the hydrate structure. In sediment-
 2 rich zones (typically represented in Fig. 4 by zone B or C), single-point Raman spectra show
 3 many peaks in the range of 800 cm^{-1} to 3100 cm^{-1} (Fig. 5). Specifically, two main
 4 contributions occurred at $\sim 1155 \text{ cm}^{-1}$ and $\sim 1521 \text{ cm}^{-1}$ which are characteristic of the C-C
 5 stretching ν_3 and ν_1 of the main polyene chain of carotenoids, respectively. Carotenoids are
 6 known to exist widely in deep-seafloor natural products and have strong recognizable
 7 resonance Raman peaks (Urmos et al., 1991; Withnall et al., 2003; Zhang et al., 2010).



8
 9 **Fig. 5:** Optical image of a sediment-rich zone (typically represented in Fig 4, B, or C) and corresponding Raman
 10 spectrum in the 200-3600 cm^{-1} spectral region of the NGH sample. The point on the optical image corresponds
 11 to the position where the Raman spectrum (yellow inset) was collected. Wavenumbers indicated in red
 12 correspond to the contribution of β -carotene. The inset in the spectrum shows the characteristic peak of methane
 13 molecules trapped in the NGH.

14 The position of the ν_1 band (at 1521 cm^{-1}) depends on the effective conjugation length
 15 (number of double carbon-carbon lengths) and can be helpful to identify the corresponding
 16 conformer. The position of the ν_1 band is consistent with the presence of β -carotene in the
 17 NGH, and spectra collected at distinct positions indicate that it is distributed heterogeneously
 18 in the analyzed sample. This compound may result both from dissolved species and small
 19 solid particles of degraded shells or fine-grain organic material recovered from the seafloor.
 20 Other peaks observed between 800 and 3100 cm^{-1} (Fig. 5, wave-numbers indicated in red)
 21 can be attributed to β -carotene (Parker et al., 1999). The signal of CH_4 trapped in the NGH is

1 detected concomitantly at $\sim 2902\text{ cm}^{-1}$ and $\sim 2913\text{ cm}^{-1}$ (see inset in Fig. 5). It is worth noting
 2 that the β -carotene signal may hinder minor contributions originating from SO_4^{2-} or CO_3^{2-}
 3 ions (respectively at 985 cm^{-1} and 1088 cm^{-1}) of electrolytes that are often reported in NGHs
 4 (Du et al., 2018; Zhang et al., 2017).

5

6 *4.2.b Raman signature of the sediment-free zone*

7 Two representative Raman spectra of the series (Fig. 6a and 6b) collected at the
 8 surface of a light-grey zone (typically represented in Fig 4, A) show the well-known signature
 9 of methane with a band doublet at $\sim 2903\text{ cm}^{-1}$ and 2914 cm^{-1} attributed to C-H stretch of CH_4
 10 trapped in both the large cage (LC) and the small cage (LC) of the NGH structure,
 11 respectively (Chazallon et al., 2007; Sum et al., 1997) (Table 2).

12 **Table 2:** Raman spectral positions of the molecules CH_4 , N_2 and H_2S in the hydrate and the free gas phase

13

<i>Position of the Raman bands (cm^{-1})</i>	<i>CH_4</i>	<i>N_2</i>	<i>H_2S</i>
<i>Hydrate</i>	~ 2903 (Large cage) ^a	2323.5 ^b	2593 (Large cage) ^{a,c}
	~ 2914 (Small cage) ^a		2604 (Small cage) ^{a,c}
<i>Free gas</i>	2916 ^c	2329 ^a	2611 ^c

14 ^a Observed in the present study

15 ^b The discrimination between the large and the small cages for the nitrogen molecules is not achievable with the
 16 present spectral resolution (Chazallon and Pirim, 2018).

17 ^c Also reported in (Chazallon et al., 2007).

18

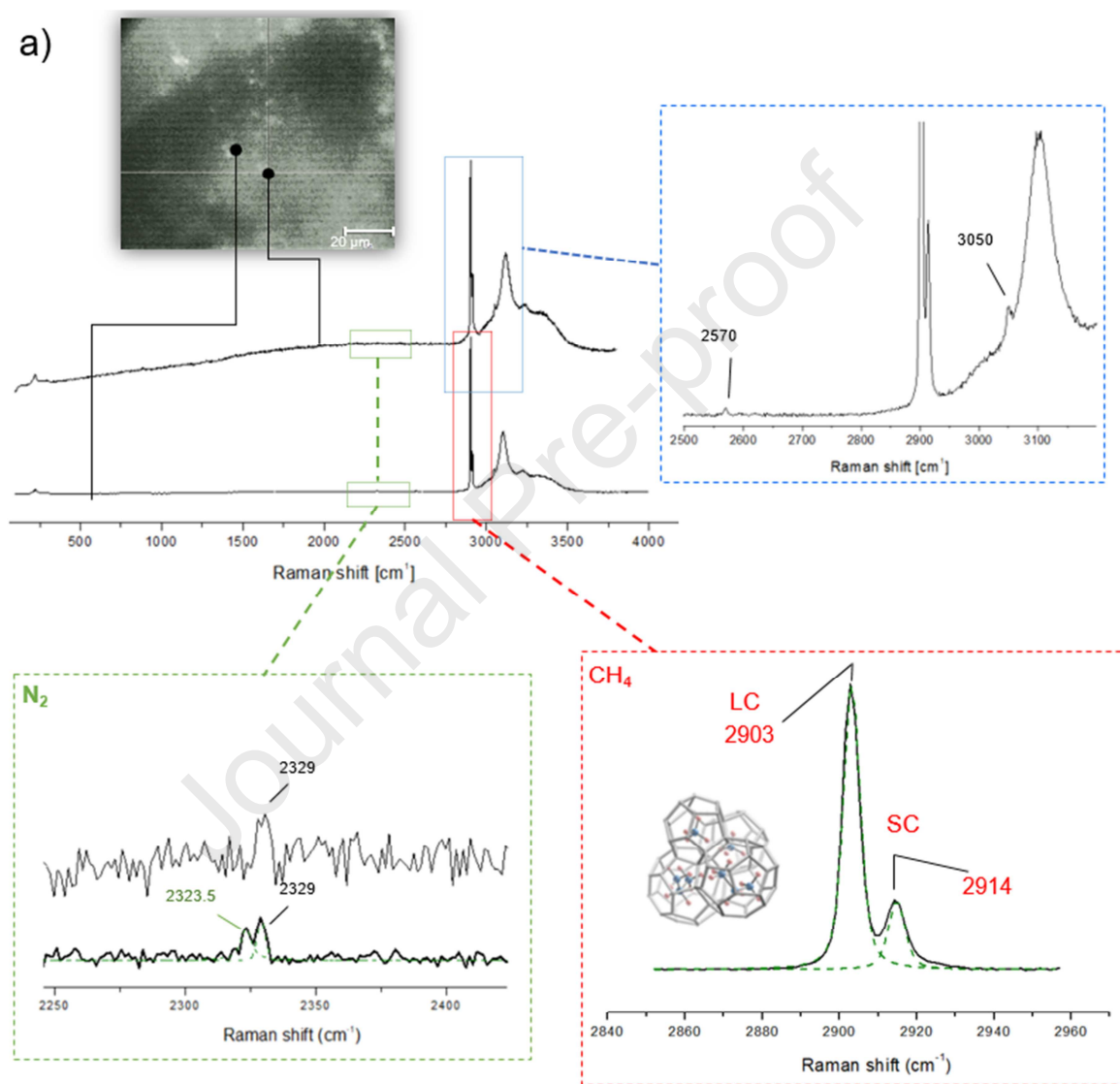
19 The peak frequencies (and for relative integrated intensity ratio, see below) indicate a
 20 structure sI which is in agreement with the compositional analysis of the hydrate-bound gases
 21 (see Table 1) with a strong methane dominance.

22 On some other parts of the investigated light-grey zone, single-point Raman spectra
 23 show, in addition to methane peak, the band characteristic of nitrogen trapped in the NGH,
 24 which emerges at $\sim 2323.5\text{ cm}^{-1}$ (Fig. 6a, inset N_2). This band is downshifted relative to that of
 25 free nitrogen gas occurring at $\sim 2329\text{ cm}^{-1}$ (Chazallon et al., 1998; Chazallon and Pirim,
 26 2018) (Table 2). Nitrogen molecules are apparently heterogeneously distributed in the NGH
 27 as the signature is not systematically observed on the probed positions (Fig. 6a, inset N_2 upper
 28 spectrum with only free nitrogen gas).

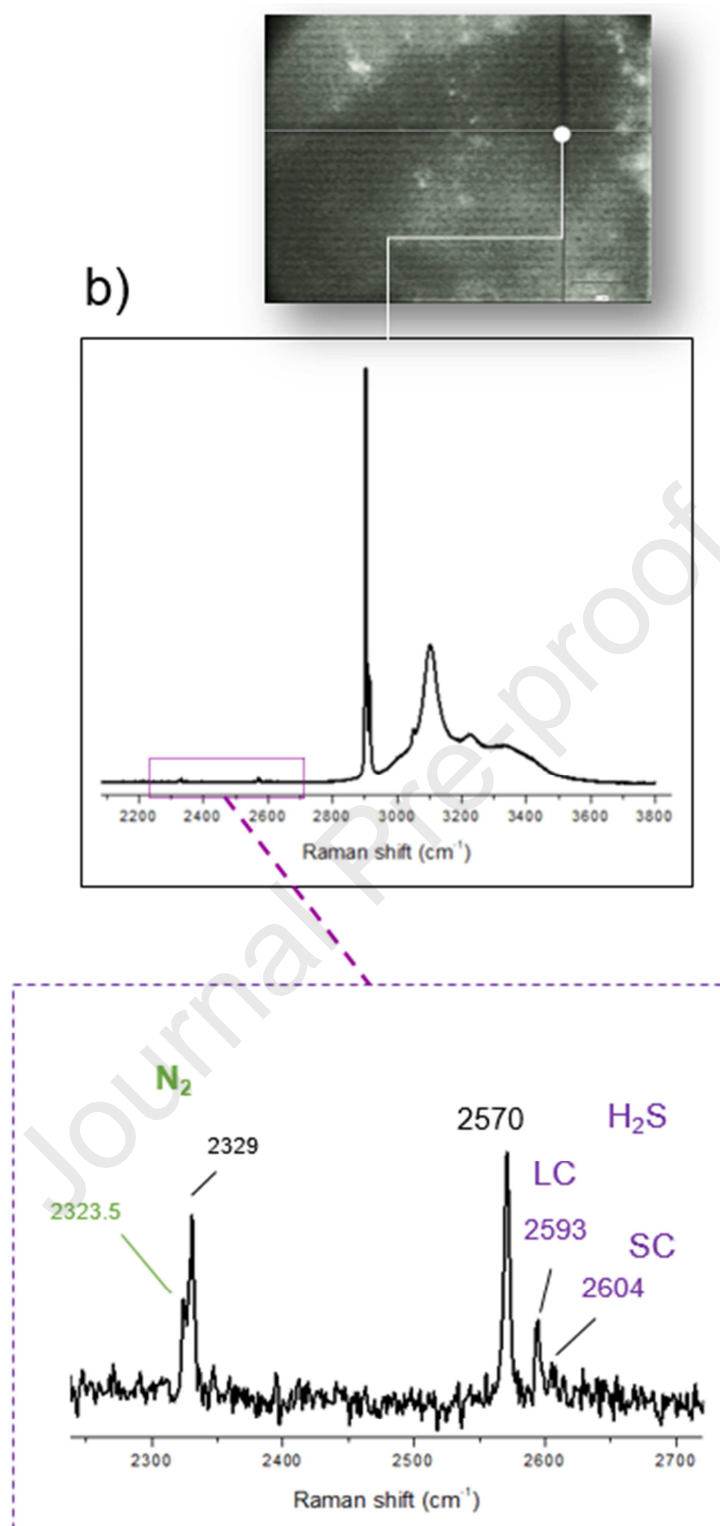
1 Molecular H₂S trapped in the NGH structure (Fig. 6b) can be identified at other
2 distinct positions (see picture in Fig. 6b), with peaks observed at ~2593 cm⁻¹ (LC)
3 cm⁻¹ (SC) that appear simultaneously with the peaks of the trapped N₂ and CH₄ (Table 2).

4

5



6



1

2 **Fig. 6:** Typical spectra collected from single-point Raman analysis of the NGH. The optical images are taken
 3 from a light-grey zone (sub-sample of the NGH's piece of Fig. 4 A) and the connected-lines show the positions
 4 at which the Raman spectra have been collected. The attribution of guests trapped in the large cage (LC) and
 5 small cage (SC) of the NGH structure I is shown in the insets (see text for details). All insets are baseline
 6 corrected: a) CH_4 (red inset) trapped into the NGH (LC peak at 2903 cm^{-1} and SC peak at 2914 cm^{-1}). Nitrogen
 7 trapped in the NGH has a single peak at 2323 cm^{-1} (N_2 , green inset lower spectrum) and free N_2 gas peak (free

1 N₂ gas from the background atmosphere) is at 2330 cm⁻¹ (N₂, green inset upper spectrum). Note also the
2 occurrence of CH₄ band overtones (2ν₄ and 2ν₂, (Chazallon et al., 2007)) (blue inset) and contribution of the
3 water lattice observed in the range 3000-3800 cm⁻¹ (O-H stretching, blue inset) and below 400 cm⁻¹
4 (translational O---O vibration) (main spectrum). b) Single point Raman spectrum showing molecular H₂S co-
5 included in the NGH (LC at 2593 cm⁻¹, SC at 2604 cm⁻¹) with N₂ (2323 cm⁻¹) (purple inset) and CH₄ (main
6 spectrum) (see text for details and Table 2).

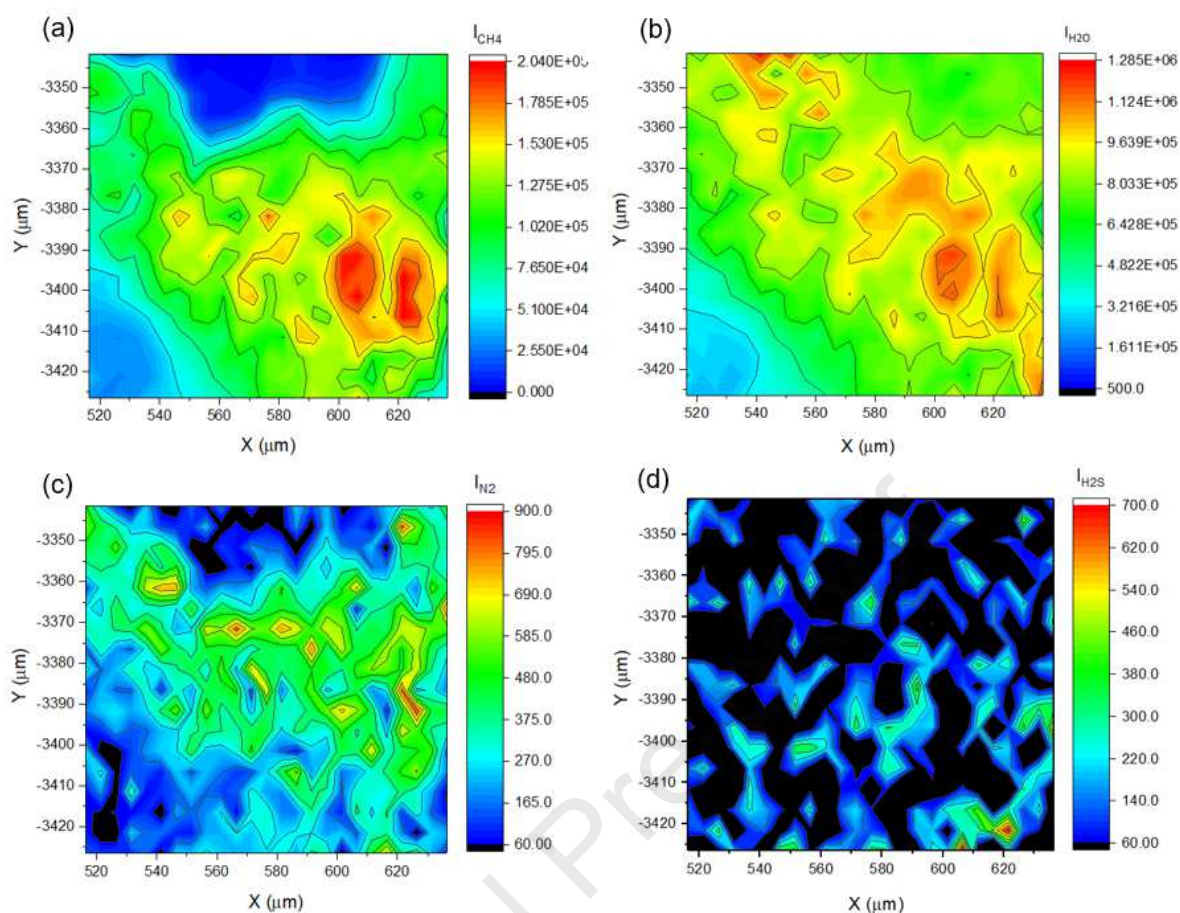
7 The interpretation of all the spectra suggests that the NGH has a heterogeneous
8 composition: with the signature of CH₄ only, CH₄ + N₂ simultaneously, or even CH₄ + N₂ +
9 H₂S depending on the position probed by the laser (see pictures in Fig 6a and 6b). It is worth
10 noting that neither CO₂ nor C₂H₆ (ethane) and C₃H₈ (propane) were detected by Raman in the
11 hydrate phase, probably because their concentration (≤ 0.05 mol%) is too low to be observed
12 with the present configuration of the instrument. Slightly different trends are observed in
13 other subsamples that appear to contain less N₂ (see supplementary material).

14

15 *4.3 Spatial variability of the NGH's composition from 2D Raman images*

16 *4.3.a Spatial variability of the guest's distribution*

17 2D-Raman mappings are applied on several parts of the sample surfaces to obtain a
18 quantitative picture of the spatial variability of the NGH composition and guests' distribution.
19 This zone was selected independently from the position where the single point Raman spectra
20 have been collected. First, a light-grey zone (represented typically in A Fig. 4) close to a
21 sediment-rich zone (typically represented in C Fig. 4) with a relatively even surface is
22 selected. Therefore, no specific cautions were taken to avoid the 'out of focus' zone during
23 the mapping process of the laser beam, and the instrument was configured with a large depth
24 of field (entrance slit of 65 μm). The zone is scanned in x and y directions with a step of 5 μm
25 (20 s/spectra), using the objective x50. Depending on the size of the zone (typically of ~ (120
26 x 85) μm²), maps of 400 to 700 complete spectra in synchro-scan mode are recorded. The
27 color-coded images represent the values of a selected parameter (here, the integrated
28 intensity) from a Raman band of each spectrum of the map.



1
 2 **Fig. 7:** Intensity distribution (integrated intensity after baseline correction) images from a Raman map (120×85)
 3 μm^2 of a selected sub-sample of the NGH. Color scale on the right of each image represents the variation of the
 4 integrated intensity of selected Raman bands for (a) CH_4 (range: $2859\text{-}2950 \text{ cm}^{-1}$), (b) H_2O ($2950\text{-}3700 \text{ cm}^{-1}$),
 5 (c) N_2 ($2321\text{-}2326 \text{ cm}^{-1}$), (d) H_2S ($2590\text{-}2606 \text{ cm}^{-1}$). Note that the value on the ranges (scale) are different
 6 despite the same color. See text for details.

7 In Fig. 7, the Raman maps show the integrated intensity of the bands corresponding to
 8 CH_4 , H_2S , N_2 , and H_2O of the NGH. The signal of ethane and propane was too low to be
 9 detected with the present configuration of the instrument. Note that a baseline correction was
 10 applied automatically on each molecular spectral range of interest, and a post-processed
 11 verification was performed visually for each spectrum. Such maps highlight the spatial
 12 variability of the different components (see also supplementary material). As expected,
 13 methane and water are present over the whole investigated scanned area (Fig. 7a and 7b). The
 14 single species map of CH_4 and H_2O shows several maxima at certain points around (x:y, 605
 15 to 620: -3410 to -3390), while blue tints at both the top and the bottom left of the CH_4 -map
 16 (Fig. 7a) are indicative of relatively lower CH_4 signal intensity. The N_2 signal is weaker but

1 follows the same distribution as CH₄, with less N₂ at the top and the bottom left of the map
2 (blue color, Fig. 7c)).

3 Furthermore, the H₂S contribution is weaker than N₂ with maxima distributed
4 heterogeneously on the map, whereas dark areas (black) imply the absence of the H₂S signal
5 (Fig. 7d). It should be noted that earlier work argues that the heterogeneous composition of
6 NGH samples collected at the Cascadia margin was a result of a variation in the availability
7 the hydrate-forming gas (CH₄ and H₂S) which is closely related to hydrocarbon fluxes
8 (Schicks et al., 2010). We also believe that such variability in the composition of the gases
9 supplying the hydrate deposit may be responsible for the heterogeneity observed in our
10 hydrate samples. The main processes that generate hydrogen sulfide in upper marine
11 sediments, as either ionized species or free gas, are Anaerobic Oxidation of Methane (AOM)
12 and Sulfate Organo-clastic Reduction (OSR) (Claypool and Kaplan, 1974; Froelich et al.,
13 1979; Reeburgh, 1976) and they take place above the gas hydrate occurrence zone (GHOZ).
14 While H₂S is involved in the precipitation of several iron-bearing minerals (especially pyrite,
15 FeS₂) (Canfield et al., 1992; Jørgensen et al., 2004; Ruffine et al., 2021) show that H₂S
16 concentration of the pore water decreases near-zero values within the first meter of sediment
17 and pyrite is present in very small amounts. Thus, H₂S is largely consumed above the GHOZ
18 and a small amount would remain to be enclathrated as hydrate, as the distance between
19 AOM, OSR, and the GHOZ is short and less than 1 m. Besides, deeply sourced hydrogen
20 sulfide can originate from thermogenic gas reservoirs (Machel, 2001; Machel et al., 1995;
21 Ruffine et al., 2018) or brines that are enriched in this compound (Commeau et al., 1987).
22 However, previous studies have shown that the limnic sediment is characterized by a lower
23 salinity (Ruffine et al., 2021; Soulet et al., 2010). Therefore, the seepage of brine is unlikely
24 in the study area. The contribution of thermogenic gas sources cannot be discarded since the
25 origin of propane is unclear. Thus, the local heterogeneous distribution of H₂S in the hydrates
26 may result from changes in the migration process of this compound from its source to the
27 hydrate occurrence zone.

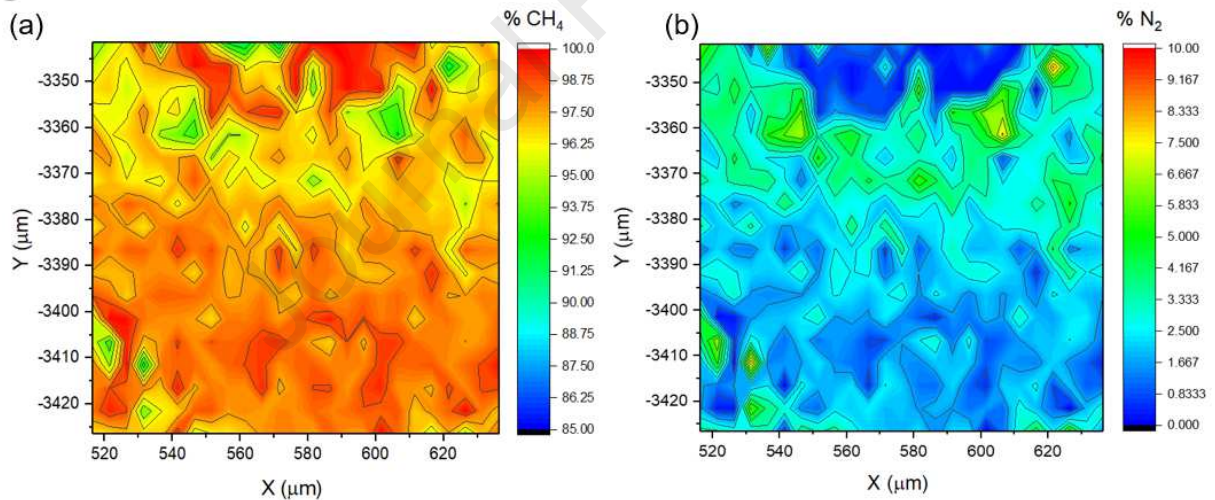
28

29 *4.3.b Spatial variability of the NGH's composition*

30 From the intensity maps generated in Fig. 7, we derived quantitative information on the
31 relative composition of the molecular guest components in the NGH as follows:

$$X_i = \frac{\theta_i}{(\theta_{CH_4} + \theta_{N_2} + \theta_{H_2S})} = \frac{A_i}{F_i/F_i^{host}} \times \left[\frac{A_{CH_4}}{F_{CH_4}/F_{CH_4}^{host}} + \frac{A_{N_2}}{F_{N_2}/F_{N_2}^{host}} + \frac{A_{H_2S}}{F_{H_2S}/F_{H_2S}^{host}} \right]^{-1} \quad (1)$$

where X_i is the molar fraction (mol%) of the guest in the NGH (with $i = CH_4, N_2, \text{ or } H_2S$) while the total cage occupancy of a certain species i derived from the Raman spectra is: $\theta_i = \frac{A_i \times 46}{8 \times A_i^{host} \times F_i/F_i^{host}}$ in structure I. A_i represents the integrated intensity of the Raman bands attributed to guest i and A_i^{host} the integrated intensity of the water contribution (O-H stretch). This latter is assumed to be independent of the engaged guest species for the same pixel (spectrum) of the map and is therefore simplified in the calculation of the ratio of equation (1). Then, the relative F-factors (guest to water) F_i/F_i^{host} in (1) are taken from the tabulated values reported for N_2 (0.13), CH_4 (1.0685, average value) (Qin and Kuhs, 2015), and of H_2S (1.372), (Yang et al., 2019). F_i (or F_i^{host}) represent the Raman quantification factor of the species i and gathers the information on the Raman cross section of i at a certain wavelength of the excitation laser source and on the instrumental efficiency of the optical and electronic response.



14

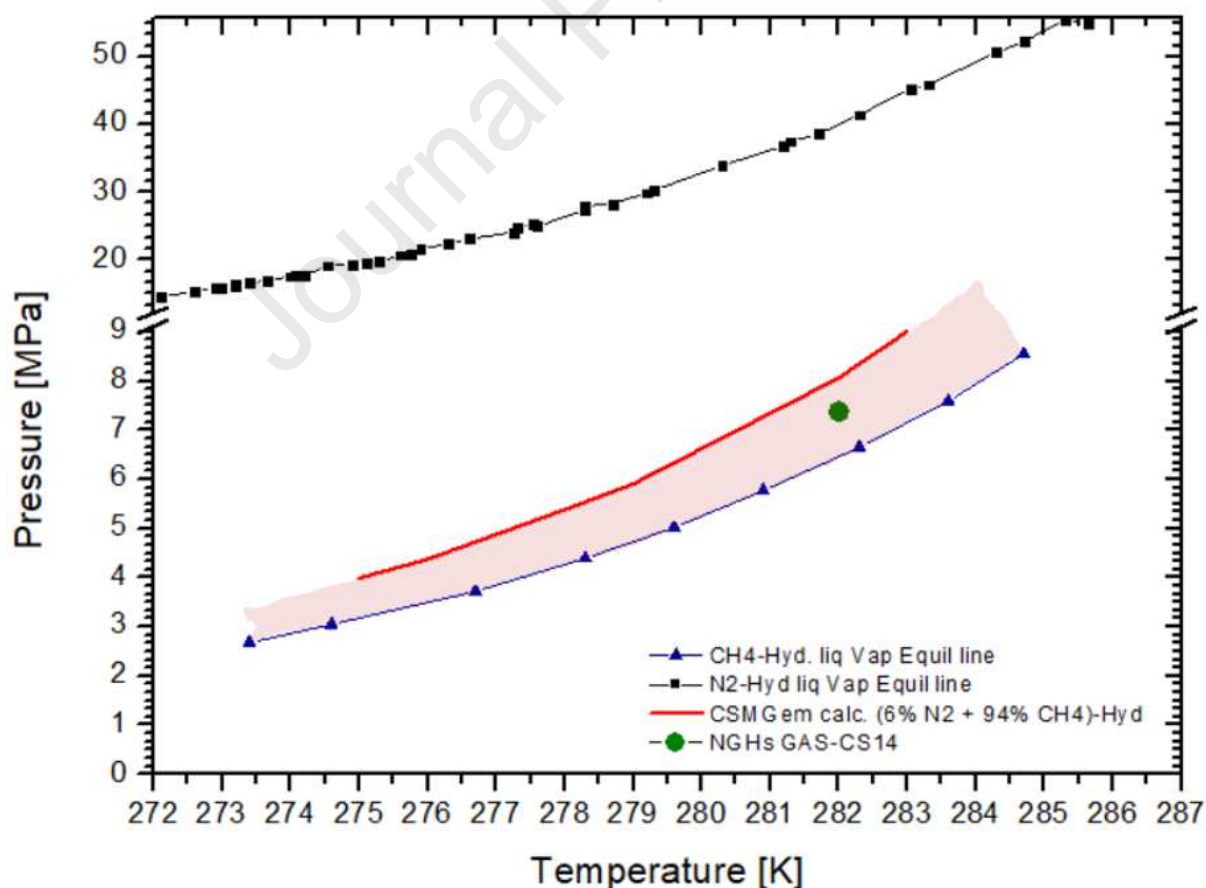
Fig. 8: Spatial variation of the guest molar fraction (mol%) (see equation (1)) in the NGH from the Raman map (120 x 85) μm^2 of a selected sub-sample. The color scale on the right of each image represents the variation of the integrated intensity of the selected Raman bands for (a) CH_4 (range: 2859-2950 cm^{-1}), (b) N_2 (2321-2326 cm^{-1}). Note the yellow-green area in map (a) (from (x:y, 520:-3360) to (x:y, 630:-3360)) has its counterpart in map (b) zone (green-light blue).

Fig. 8 shows a color-coded map of the guest molar composition (mol%) of CH_4 and N_2 in the NGH using equation (1). Some parts of the maps clearly exhibit a relative depletion of the CH_4 molar fraction ($< \sim 97$ mol%) together with a relative enrichment with N_2 ($> \sim 6$

1 mol%). This can typically be seen in the yellow-green zone of Fig. 8a from (x:y, 520:-3360)
 2 to (x:y, 630:-3360), or equivalently in the green-light blue zone of Fig. 8b. This indicates that
 3 while our NGH samples show an optically homogeneous appearance (typically a light-grey
 4 area as in Fig. 4 A), the relative guest composition shows a spatial variability (at least at the
 5 micron-scale).

6 To investigate how the presence of nitrogen may impact the stability of the NGH, the
 7 equilibrium line of a gas hydrate containing 6% N_2 and balanced CH_4 was simulated (Fig. 9,
 8 red line) using CSMGem (Sloan and Koh, 2008)). The desired nitrogen composition in the
 9 hydrate phase was obtained by processing the equilibrium points with different feed gas ratios
 10 $N_2:CH_4$. In the simulation, only pure water was used (no salinity). The result was compared
 11 with the equilibrium line of the pure CH_4 -hydrate (hydrate + vapor + liquid water equilibrium
 12 line (Fig. 9, blue triangles)). Also, the equilibrium line of the pure N_2 -hydrate was plotted
 13 (Fig. 9, black squares) for comparison.

14



15

1 **Fig. 9.** Simulated (CSMGem) equilibrium line of a gas hydrate containing 6% N₂ + 94% CH₄ (red line). Only
2 pure water is considered for the simulation (no salinity). Comparison with the equilibrium line (hydrate + vapor
3 + liquid water) of pure CH₄-hydrate (dark-blue up-triangle), pure N₂-hydrate (black squares): literature data from
4 Adisasmito et al. (1991) and van Cleef and Diepen (1965). The green filled circle represents the conditions (282
5 K, 7.5 MPa) at the sea floor where the NGH was collected.

6 The presence of nitrogen shifts the dissociation line to higher pressures or lower
7 temperatures (red area on the plot Fig. 9). In other words, the stability of an NGH containing
8 6% N₂ is lower than that of a gas hydrate containing 100% CH₄. Note that the N₂ enrichment
9 up to ~6 mol% is an upper concentration limit for N₂ (Fig. 8) at a certain location of the
10 sample and the value of ~0.29 mol% N₂ reported above (section 4.1) constitutes an average
11 concentration which will provide an equilibrium line (not calculated here) much closer to the
12 CH₄-hydrate equilibrium line and below the NGH point (green point in Fig. 9). Moreover, the
13 formation of hydrates with (94% CH₄ + 6% N₂) requires a feed gas with an even higher
14 nitrogen content (~20% N₂ + 80% CH₄) as the N₂ selectivity at the hydrate phase is assumed
15 to be lower than that of CH₄. It appears that the thermodynamic conditions of the NGH, which
16 is expected to be that of the sea floor ~282 K and 7.38 MPa, falls outside the equilibrium line
17 of a simulated mixed hydrate of composition (94 % CH₄ + 6% N₂). This suggests that the
18 formation conditions of the NGH can be impacted by important but very local changes in
19 temperature and pressure within the sediment, and/or in gas composition or even by the salt
20 environment. Further work with synthetic binary (CH₄+N₂) mixtures would be useful to
21 elucidate how the guests are spatially distributed in the hydrate sample when starting from a
22 finite amount of gas (water-saturated conditions) (see discussion in section 4.5).

23 The concentration of H₂S is too low to be estimated with sufficient accuracy in the present
24 configuration. As mentioned above, the growth of the NGH likely took place in pore water
25 with a fluctuating composition of the dissolved N₂ and H₂S throughout the hydrate formation
26 process. These two compounds are generated at variable rates and depth in the marine
27 sediments. They can be more or less available to be enclathrated in the hydrates. Thus, the
28 composition of the hydrates may change according to the fluctuation of pore water
29 composition. Note finally that the estimated gas concentration from the single point Raman-
30 spectra shown in Fig. 6b is 98.2 mol% CH₄, 1.5 mol% N₂, and 0.3 mol% H₂S whereas, this
31 reaches ~94.3 mol% CH₄ and ~5.7 mol% N₂ in the absence of H₂S (Fig. 6a). This is in
32 agreement with the concentration range covered by the map shown in Fig. 8 and collected on
33 a distinct sample part.

1

2 *4.4 Relative cage occupancies of the NGH*

3 From the integrated intensity ratio of the C-H stretching bands of each spectrum collected
 4 in the Raman image, we derived a map of the spatial distribution of the relative cage
 5 occupancy of the CH₄ in the NGH (Fig. 10). Such results are valuable to future work aiming
 6 at improving the estimate of the amount of methane storage in the Western Black Sea hydrate
 7 deposit. Because the unit cell of sI has two small cages and six large cages with 46 water
 8 molecules, a relation between the Raman integrated intensity of the C-H bands (I_{LC} and I_{SC})
 9 and the cage occupancy ratio (θ_{LC}/θ_{SC}) is obtained by the relation (2):

$$10 \quad \theta_{LC}/\theta_{SC} = (I_{LC}/3I_{SC}) \times F \quad (2)$$

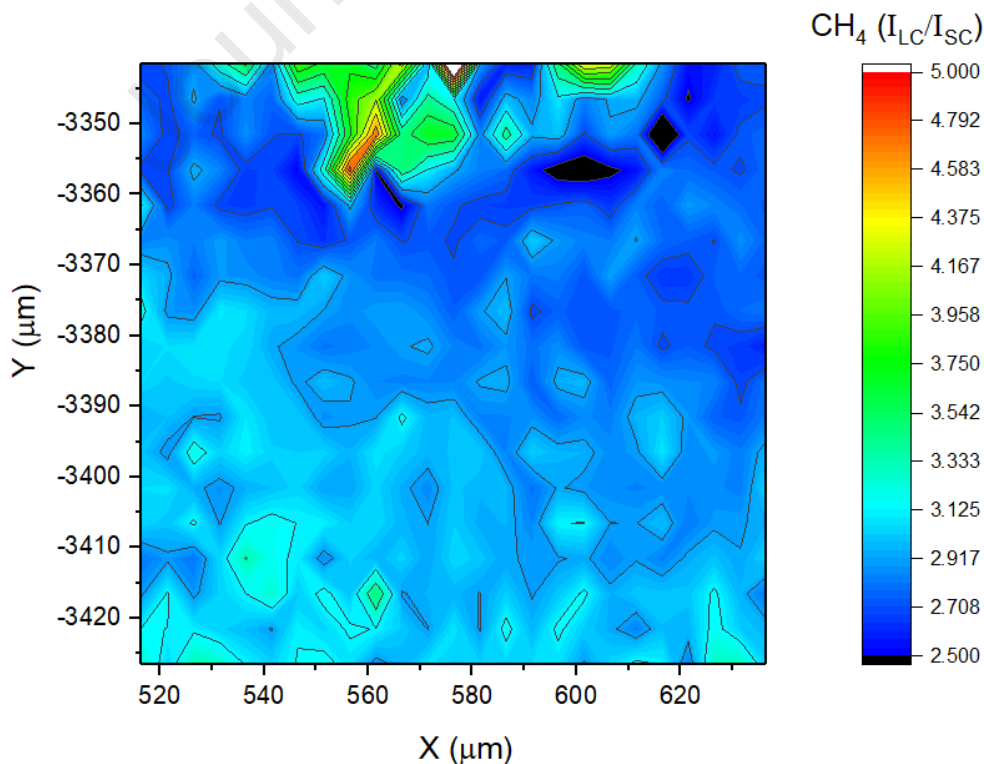
11 where $F \sim 1.08$ represents the Raman scattering cross-section ratio of methane trapped in the
 12 SC relative to the one of methane in the LC (Qin and Kuhs, 2013).

13 It is noticeable to observe that N₂-rich areas in Fig. 8b correspond to the low I_{LC}/I_{SC} ratio in
 14 Fig. 10 (dark-blue zone, Fig. 10). For example, $I_{LC}/I_{SC} \sim 2.3$ means that the cage occupancy
 15 ratio is $\theta_{LC}/\theta_{SC} \sim 0.82$ and thus the LCs are less populated by CH₄ molecules than the SCs
 16 in structure sI. This is attributed to the fact that a certain percentage of the LC is occupied by
 17 N₂ molecules. When a very small amount (or no amount) of N₂ is detected, the I_{LC}/I_{SC}
 18 increases to ~ 3.5 , i.e., a cage occupancy ratio of $\theta_{LC}/\theta_{SC} \sim 1.26$.

19 Our reported values are the first micron-scale structural study of gas hydrate sample from
 20 the Black Sea, it is then interesting to compare the results with those obtained on other NGHs
 21 from the literature (Table S1 in supplementary material) or synthetic pure methane hydrates.
 22 It has often been reported that in marine gas hydrates the LC is almost filled with cage
 23 occupancy higher than 90%, whereas the SC remains partially filled around 80% for most
 24 marine hydrates (see Liu et al. (2012) and reference therein). It is also found that the relative
 25 cage occupancy (θ_{LC}/θ_{SC}) values vary strongly in NGH according to the geological area
 26 (Table S1) and the nature of the hydrocarbons co-encased in the structure. The analyses from
 27 offshore India, Ullung Basin, Malik 5L-38, Mount Elbert Well, Gulf of Mexico, Lake Baikal
 28 indicate that the NGH consist of various guest molecules (Bahk et al., 2009; Kida et al., 2009;
 29 Klapp et al., 2010; Kumar et al., 2008; H. Lu et al., 2011a, 2011b; Z. Lu et al., 2011;
 30 Ripmeester et al., 2005). The lowest ratios reported are $\theta_{LC}/\theta_{SC} \sim 0.91$ in Mount Elbert well,

1 and Malik 5L-38 well Alaska (onshore) and ~ 1.09 in Pearl River Mouth basin (PRM basin,
2 offshore south China).

3 In comparison, in artificial methane hydrates, it was found that θ_{LC}/θ_{SC} decreases slightly
4 (from ~ 1.15 to 1.10) as pressure increases from 3.5 to 15 MPa along isotherm 268 K, that is,
5 when exploring the stability field of methane hydrates. This was attributed to a pressure-
6 dependent change of the relative size of the SCs and LCs (Chazallon and Kuhs, 2002; Qin and
7 Kuhs, 2013). In contrast, the ratio θ_{LC}/θ_{SC} was found to be independent of pressure along the
8 three-phase equilibrium curve between 5 and 60 MPa, with $I_{LC}/I_{SC} \sim 3.9$ (i.e., $\theta_{LC}/\theta_{SC} \sim 1.28$)
9 (Moryama et al., 2015). In both cases, the SC occupancy was found to be lower (and constant
10 ($\sim 80\%$) even below 20 MPa) than that of the LC with 100% occupancy. Since our NGH was
11 collected in conditions (~ 282 K and ~ 7.5 MPa) close to the three-phase equilibrium curve of
12 pure (sI structure) CH_4 -hydrate (~ 1.5 MPa above the equilibrium line), the expected I_{LC}/I_{SC}
13 ratio should be close to that calculated by Moryama et al. (2015). Any deviation from I_{LC}/I_{SC}
14 ~ 3.9 is then attributed either to a variation in the relative amount of minor gas components
15 mixed with methane (nitrogen in our case), or to a local change in thermodynamic conditions
16 (i.e. exploring other deeper regions in the stability field, far from the three-phase equilibrium
17 curve in the (p, T) space).



1 **Fig. 10:** Spatial variability of the Raman integrated intensity ratio of the C-H bands attributed to methane in the
2 LC and SC of the NGH containing methane and nitrogen as main gas components. See text for details.

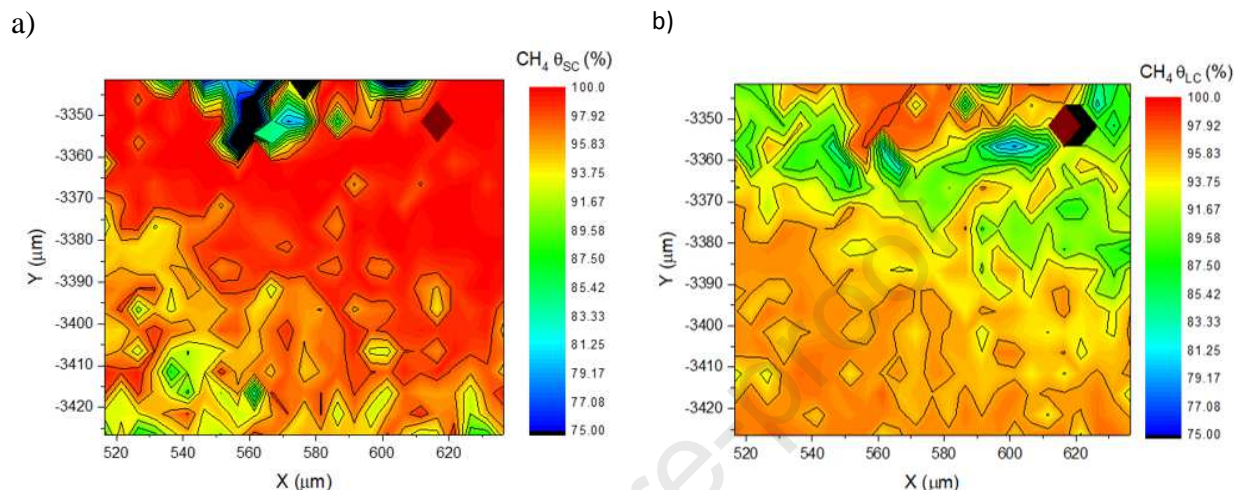
3 Very low I_{LC}/I_{SC} ratio (~ 1.4) (or $\theta_{LC}/\theta_{SC} \sim 0.5$) is found in other Raman maps (Fig. S1, Fig.
4 S2, and Fig. S3 in supplementary material) where only CH_4 is detected. Earlier studies (Yeon
5 et al., 2011) have shown that abnormal cage occupancy ratio up to ~ 7.1 ($\theta_{LC}/\theta_{SC} \sim 2.4$) may
6 occur when NGH are formed from clay-rich (Na-montmorillonite) sediments near the
7 seafloor. This is attributed to sodium ions that compete with methane to occupy the SC of
8 structure sI. In contrast, the highest ratio measured here is $I_{LC}/I_{SC} \sim 3.9$ although clays (with
9 illite $> 90\%$ w/w and kaolinite $\sim 5\%$ w/w) are the dominant minerals of the sediment at the
10 area where the core was collected (Ruffine et al., 2021), no evidence of montmorillonite was
11 found. Therefore, an analogy with what has been observed with Ca- and Na-montmorillonite
12 needs to be developed.

13 Furthermore, electrolyte solutions (3.5 wt% NaCl in a sediment-free solution) are known to
14 have a negligible effect on the cage occupancy of CH_4 -hydrates ($I_{LC}/I_{SC} \sim 3.8$) (Moryama et
15 al., 2015). Similarly to the case of hydrates formed from pure water (Qin and Kuhs, 2013), the
16 ratio slightly decreases ($I_{LC}/I_{SC} \sim 3.2$) at higher pressure (10 MPa and 274 K), i.e., deep in the
17 stability field, in a salt environment (4 wt% NaCl) (Shin et al., 2017). Thus, sodium ions
18 present in the original aqueous solution do not impact cage occupancy in artificial hydrates.
19 Nevertheless, the Black Sea has a lower salinity level (~ 1 wt% measured in the pore water)
20 than the known mean value of sea water (~ 3.5 wt%) as a result of ongoing seawater
21 infiltration within the limnic sediment of the Black Sea since the reconnection of this sea with
22 the Atlantic-ocean. This progressive downward increase in pore-water salinity changes the
23 chemical and mineral properties of sediment through ion-exchange and redox processes
24 (Ruffine et al., 2021). These changes in sediment properties may also affect the mechanism of
25 hydrate formation. Accordingly, a more detailed study of the impact of sediment property
26 changes due to seawater infiltration on cage occupancy appears necessary in the Black Sea
27 where salinity decreases downward from 20 to 2 psu at around 25 mbsf (Riboulot et al., 2018;
28 Ruffine et al., 2021; Soulet et al., 2010). This salinity value of 2 psu is lower than the 6 psu
29 measured by (Manheim and Chan, 1974) within the first 8 m of sediment.

30

31 *4.5 Hydration numbers and correlation with the estimated total amount of methane*

1 From the results of the previous map measuring relative cage occupancy (Fig. 10), we derived
 2 the absolute values of cage occupancies using the van der Waals and Platteuw theory (van
 3 der Waals and Platteuw, 1958) assuming that the chemical potential difference between ice
 4 and the hypothesized empty clathrate lattice of sI is $\Delta\mu_w^\circ = 1297 J/mol$ (Davidson et al.,
 5 1986b) and the temperature is fixed at 282 K (the sea floor temperature).



6
 7 **Fig. 11:** Spatial variation of cage occupancies in the NGH structure I derived from the Raman data and the van
 8 der Waals and Platteuw model a) SC (small cage) occupancy, b) LC (large cage) occupancy. Note that the
 9 filling of the SC approaches 100% in most areas whereas the filling of the LC is around 85-95%. See text for
 10 details.

11
 12 The map of Fig. 11a displays the spatial variation of the CH_4 occupancy in the SC that shows
 13 significant variation from $\sim 75\%$ (dark color) to 100% (red color) in the analyzed zone. It
 14 should be noted that the part of the map where the CH_4 -SC occupancy is between $\sim 98-100\%$
 15 (Fig. 11a) corresponds to an N_2 -rich area (Fig. 8b). In contrast the CH_4 -LC occupancy never
 16 reaches 100% (Fig. 11b) and the orange to brown-colored area with CH_4 -LC occupancy of
 17 $\sim 93-95\%$ corresponds to the N_2 -depleted area (Fig. 8b). Moreover, the green-colored area
 18 (Fig. 11b) with CH_4 -LC occupancies of $\sim 85\%$ corresponds to an N_2 -rich area (Fig. 8b). The
 19 comparison between the concentration map (Fig. 8) and the map of Fig. 11 suggests that the
 20 occurrence of N_2 guest molecules have an impact on the global methane cage occupancy with
 21 N_2 preferentially populating the LC of the structure I. This result is unexpected when
 22 considering the equilibrium cage occupancies obtained during the simulation by CSMGem
 23 (Fig. 9) of the equilibrium line trajectory with corresponds to equilibrium cage occupancies
 24 for CH_4 of $\theta_{LC} \sim 90\%$ and $\theta_{SC} \sim 77\%$. The guest distribution in the NGH may compensate the

1 less good stabilization due to the large cages being occupied by N_2 . Therefore, we suggest
2 that the distinct guest distribution observed here may play a role in the stability of the N_2 -rich
3 area of the NGH. It should be noted that the earlier work of Sum et al. (1997) does not show
4 any variation in absolute methane cage occupancy. The authors started to form their synthetic
5 mixed CH_4 - N_2 -hydrate samples from a CH_4 - N_2 feed gas composition as low as $y_{CH_4} \sim 58\%$.
6 This may be explained by the consumption of the milder hydrate former first (with a CH_4 -
7 enriched hydrate), followed by the formation of spatially separated secondary pure hydrate
8 crystals (N_2 -enriched hydrate). Further investigation of the influence of nitrogen on methane
9 cage occupancy using synthetic hydrates would be helpful to elucidate the distribution of
10 nitrogen in the cages of this mixed hydrate system. It should be noted that N_2 and CH_4
11 molecules possess similar sized properties with guest-to-cavity diameter ratios of ~ 0.8 (N_2) to
12 0.86 (CH_4) for the SC and ~ 0.7 (N_2) to 0.74 (CH_4) for the LC of sI (Sloan and Koh, 2008).
13 According to the guest-to-cavity diameter rule (i.e., guest-to-cavity diameter ratio < 0.76 or $>$
14 1 does not allow cage stabilization), both molecules fit the SC better and are expected to
15 occupy preferentially this cage type. This makes the prediction of the preferential partitioning
16 within the cages relatively unsure using simple additive effects, specifically when a structure
17 sI former (CH_4) is mixed with a sII former (N_2). The guest-host interactions likely change in
18 the mixed system maintaining a preferential stable structure with adapted cage occupancy.

19 How this result will affect the global estimate of methane is a critical question. As mentioned
20 previously, the global estimates of methane gas trapped in NGH are based on several
21 parameters that are functions of geological conditions. One of these concerns the volumetric
22 conversion factor that has often been calculated by assuming (based on structure sI) a mean
23 cage occupancy of 85%, i.e. a hydration number of methane hydrates of ~ 6.75 ($= 46/(0.85 \times$
24 $8)$), and therefore a value of $\sim 164 \text{ m}^3$ of methane per m^3 of hydrate is being typically used
25 (Boswell and Collett, 2011; Kvenvolden, 1998). We derived an upper estimate of the
26 volumetric conversion factor of our NGH which can contain up to ~ 6 mol% of N_2 according
27 to the spectral map presented in Fig. 8. Given the CH_4 cage occupancy calculated in the map
28 of Fig. 10 at the corresponding composition of 6% N_2 , one derives that 1 m^3 of such NGH
29 will instead contain $\sim 153 \text{ m}^3$ of CH_4 . For this calculation, we used the lattice constant of CH_4 -
30 hydrate provided at 282 K by Kuhs et al. (2004) as $a = 11.98 \text{ \AA}$ and a cage occupancy of
31 $\theta_{LC} \sim 0.84$, $\theta_{SC} \sim 0.99$ (hydration number of ~ 6.55) (from Fig. 11). Note that both the lattice
32 constant and the cage occupancies adopted in this calculation are critical parameters. A value
33 of $\sim 148 \text{ m}^3$ is obtained with the lattice constant $a = 11.98 \text{ \AA}$ and the mean cage occupancy of

1 85% (Boswell and Collett, 2011). To summarize, the spatial variation of the methane cage
2 occupancy which is reminiscent of the presence of additional minor guest-gas components
3 (mainly N₂) in the NGH may affect significantly the volumetric conversion factor and
4 therefore the global estimate of methane in NGH.

5

6 **5. Conclusion**

7 NGH collected during the Ghass cruise (2015) in the Black Sea onboard the *R/V*
8 *Pourquoi pas?* have been analyzed using different complementary techniques: gas
9 chromatography and micro-Raman spectroscopic imaging. The results showed that the
10 hydrate-bound light hydrocarbons are of microbial origin, and generated from the carbon-
11 dioxide reduction process. Methane is overwhelmingly present, followed by nitrogen (with
12 some enrichment higher than 6 mol%). Carbon dioxide, as well as ethane and propane, are
13 minor elements to traces. The Raman signal of a small amount of hydrogen sulfide (H₂S) is
14 also detected in the NGH, which supposes that it may be found locally in the surrounding
15 water at a higher concentration level than ethane, propane, and carbon dioxide, as they were
16 not identified in the hydrate phase. This important result indicates that hydrates are potential
17 sinks for H₂S generated from seawater-sulfate reduction. Single point Raman spectra allow
18 the identification of distinct guest components in the NGH embedded in the sediment, while
19 2D-Raman images reveal the heterogeneous distribution of the guest concentration at the
20 microscale, with methane being the main component. The spatial variability of the CH₄ cage
21 occupancy is reported for the first time and can be correlated with the inclusion of nitrogen
22 that is shown to preferentially occupy the LC of the structure I. Other components
23 (carotenoids) often identified in pore water during field experiments (Zhang et al., 2010) are
24 identified here in the well-preserved recovered samples. The small-scale heterogeneities of
25 the sample composition, with addressed statistical issues, highlight the importance to conduct
26 2D-Raman images when characterizing natural gas hydrate samples. Furthermore, from the
27 Raman map of the CH₄ cage occupancies in the NGH, it was derived that the occurrence of
28 minor components, even at low concentrations, could impact the volumetric conversion factor
29 of CH₄ gas. Typically, hydrates including N₂ at 6mol% have a lower volumetric conversion
30 factor than that expected in a GH containing only methane. There is also a need to
31 characterize the variation of the cage occupancy with depth within the sediment, and then
32 compare the result with the zonation of geochemical reactions, which would help to decipher

1 sources of minor guest molecules. Also, a systematic study on a larger number of NGH
2 samples from the same area would be appropriate to identify the main factors that are
3 responsible for the heterogeneity of cage occupancy and to provide meaningful insights into
4 the hydrate formation mechanism. The overall results allow to define a statistical cage
5 occupancy distribution, which, if coupled with seismic data, would allow us to refine the
6 estimation of the amount of gas trapped in the hydrate deposit.

7

8 **Acknowledgements**

9 We thank the captain and his crew on-board the *RV Pourquoi pas?* for their technical support
10 and advice. Thanks to Alison Chalm for proofreading the article. Financial support for the
11 cruise was provided by Ifremer and the European project Midas (grant agreement 603418).
12 One author (C.T.R.) thanks Lille University and the Région Hauts-de-France for support
13 through a Ph.D. grant n°17006757. This work is a contribution to the BLAME project
14 sponsored by the French National Research Agency (ANR-18-CE01-0007). This study was
15 undertaken in the frame of the French Research Consortium “GdR2026- Hydrates de gaz”.

16

17 **REFERENCES**

18

- 19 Adisasmito, S., Frank, R.J., Sloan, E.D., 1991. Hydrates of carbon dioxide and methane
20 mixtures. *J. Chem. Eng. Data* 36, 68–71. <https://doi.org/10.1021/je00001a020>
- 21 Bahk, J.J., Kim, J.H., Kong, G.S., Park, Yosup, Lee, H., Park, Youngjun, Park, K.P., 2009.
22 Occurrence of near-seafloor gas hydrates and associated cold vents in the Ulleung Basin,
23 East Sea. *Geosci. J.* 13, 371–385. <https://doi.org/10.1007/s12303-009-0039-8>
- 24 Bernard, B.B., Brooks, J.M., Sackett, W.M., 1978. Light hydrocarbons in recent Texas
25 continental shelf and slope sediments. *J. Geophys. Res.* 83, 4053.
26 <https://doi.org/10.1029/jc083ic08p04053>
- 27 Boswell, R., Collett, T.S., 2011. Current perspectives on gas hydrate resources. *Energy*
28 *Environ. Sci.* 4, 1206–1215. <https://doi.org/10.1039/C0EE00203H>
- 29 Boswell, R., Hancock, S., Yamamoto, K., Collett, T., Pratap, M., Lee, S.-R., 2020. Natural
30 Gas Hydrates: Status of Potential as an Energy Resource, *Future Energy*. Elsevier Ltd.
31 <https://doi.org/10.1016/B978-0-08-102886-5.00006-2>
- 32 Bourry, C., Charlou, J.-L., Donval, J.-P., Brunelli, M., Focsa, C., Chazallon, B., 2007. X-ray
33 synchrotron diffraction study of natural gas hydrates from African margin. *Geophys.*
34 *Res. Lett.* 34, L22303. <https://doi.org/10.1029/2007GL031285>
- 35 Bourry, C., Chazallon, B., Charlou, J.L., Pierre Donval, J., Ruffine, L., Henry, P., Geli, L.,

- 1 Çagatay, M.N., İnan, S., Moreau, M., 2009. Free gas and gas hydrates from the Sea of
2 Marmara, Turkey Chemical and structural characterization. *Chem. Geol.* 264, 197–206.
3 <https://doi.org/10.1016/j.chemgeo.2009.03.007>
- 4 Brooks, J.M., Kennicutt, M.C., Fay, R.R., McDonald, T.J., Sassen, R., 1984. Thermogenic
5 gas hydrates in the Gulf of Mexico. *Science.* 225, 409–411.
6 <https://doi.org/10.1126/science.225.4660.409>
- 7 Canfield, D.E., Raiswell, R., Bottrell, S.H., 1992. The reactivity of sedimentary iron minerals
8 toward sulfide. *Am. J. Sci.* 292, 659–683. <https://doi.org/10.2475/ajs.292.9.659>
- 9 Charlou, J.L., Donval, J.P., Fouquet, Y., Ondreas, H., Knoery, J., Cochonat, P., Levaché, D.,
10 Poirier, Y., Jean-Baptiste, P., Fourré, E., Chazallon, B., 2004. Physical and chemical
11 characterization of gas hydrates and associated methane plumes in the Congo-Angola
12 Basin. *Chem. Geol.* 205, 405–425. <https://doi.org/10.1016/j.chemgeo.2003.12.033>
- 13 Chazallon, B., Champagnon, B., Panczer, G., Pauer, F., Klapproth, A., Kuhs, W.F., 1998.
14 Micro-Raman analysis of synthetic air clathrates. *Eur. J. Mineral.* 10, 1125–1134.
15 <https://doi.org/10.1127/ejm/10/6/1125>
- 16 Chazallon, B., Focsa, C., Charlou, J.-L., Bourry, C., Donval, J.-P., 2007. A comparative
17 Raman spectroscopic study of natural gas hydrates collected at different geological sites.
18 *Chem. Geol.* 244, 175–185. <https://doi.org/10.1016/j.chemgeo.2007.06.012>
- 19 Chazallon, B., Kuhs, W.F., 2002. In situ structural properties of N₂-, O₂-, and air-clathrates
20 by neutron diffraction. *J. Chem. Phys.* 117, 308–320. <https://doi.org/10.1063/1.1480861>
- 21 Chazallon, B., Noble, J., Desmedt, A., 2017. Spectroscopy of Gas Hydrates: from
22 fundamental aspects to Chemical Engineering, Geophysical and Astrophysical
23 applications, in: Ruffine, L., Broseta, D., Desmedt, A. (Eds.), *Gas Hydrates 1:
24 Fundamentals, Characterization and Modeling of Gas Hydrates.* ISTE-Wiley, London.
- 25 Chazallon, B., Pirim, C., 2018. Selectivity and CO₂ capture efficiency in CO₂-N₂ clathrate
26 hydrates investigated by in-situ Raman spectroscopy. *Chem. Eng. J.* 342, 171–183.
27 <https://doi.org/10.1016/j.cej.2018.01.116>
- 28 Claypool, G.E., Kaplan, I.R., 1974. The origin and distribution of methane in marine
29 sediments, in: Kaplan, I. R. (Ed.), *Natural Gases in Marine Sediments.* New York, pp.
30 99–139.
- 31 Colin, F., Ker, S., Riboulot, V., Sultan, N., 2020. Irregular BSR: Evidence of an Ongoing
32 Reequilibrium of a Gas Hydrate System. *Geophys. Res. Lett.* 47, 0–3.
33 <https://doi.org/10.1029/2020GL089906>
- 34 Commeau, R.F., Paull, C.K., Commeau, J.A., Poppe, L.J., 1987. Chemistry and mineralogy of
35 pyrite-enriched sediments at a passive margin sulfide brine seep: abyssal Gulf of
36 Mexico. *Earth Planet. Sci. Lett.* 82, 62–74. [https://doi.org/10.1016/0012-
37 821X\(87\)90107-5](https://doi.org/10.1016/0012-821X(87)90107-5)
- 38 Davidson, D., Garg, S., Gough, S., Handa, Y., Ratcliffe, C., Ripmeester, J., Tse, J., Lawson,
39 W., 1986a. Laboratory analysis of a naturally occurring gas hydrate from sediment of the
40 Gulf of Mexico. *Geochim. Cosmochim. Acta* 50, 619–623. [https://doi.org/10.1016/0016-
41 7037\(86\)90110-9](https://doi.org/10.1016/0016-7037(86)90110-9)

- 1 Davidson, D., Handa, Y., Ripmeester, J., 1986b. Xenon-129 NMR and the thermodynamic
2 parameters of xenon hydrate. *J. Phys. Chem.* 90, 6549–6552.
3 <https://doi.org/10.1021/j100282a026>
- 4 Du, Z., Zhang, X., Xi, S., Li, L., Luan, Z., Lian, C., Wang, B., Yan, J., 2018. In situ Raman
5 spectroscopy study of synthetic gas hydrate formed by cold seep flow in the South China
6 Sea. *J. Asian Earth Sci.* 168, 197–206. <https://doi.org/10.1016/j.jseaes.2018.02.003>
- 7 Egger, M., Kraal, P., Jilbert, T., Sulu-Gambari, F., Sapart, C.J., Röckmann, T., Slomp, C.P.,
8 2016. Anaerobic oxidation of methane alters sediment records of sulfur, iron and
9 phosphorus in the Black Sea. *Biogeosciences* 13, 5333–5355. [https://doi.org/10.5194/bg-](https://doi.org/10.5194/bg-13-5333-2016)
10 [13-5333-2016](https://doi.org/10.5194/bg-13-5333-2016)
- 11 Egorov, V.N., Artemov, Y.G., Gulin, S.B., Polikarpov, G., 2011. Methane seeps in the Black
12 Sea: discovery, quantification and environmental assessment. *J. Black*
13 *Sea/Mediterranean Environ.* 17, 171–185.
- 14 Froelich, P.N., Klinkhammer, G.P., Bender, M.L., Luedtke, N.A., Heath, G.R., Cullen, D.,
15 Dauphin, P., Hammond, D., Hartman, B., Maynard, V., 1979. Early oxidation of organic
16 matter in pelagic sediments of the eastern equatorial Atlantic: suboxic diagenesis.
17 *Geochim. Cosmochim. Acta* 43, 1075–1090. [https://doi.org/10.1016/0016-](https://doi.org/10.1016/0016-7037(79)90095-4)
18 [7037\(79\)90095-4](https://doi.org/10.1016/0016-7037(79)90095-4)
- 19 Haeckel, M., Bialas, J., Klaucke, I., Wallmann, K., Bohrmann, G., Schwalenberg, K., 2015.
20 Gas Hydrate Occurrences in the Black Sea – New Observations from the German
21 SUGAR Project. *Fire Ice* 6–14.
- 22 Heeschen, K.U., Haeckel, M., Klaucke, I., Ivanov, M.K., Bohrmann, G., 2011. Quantifying
23 in-situ gas hydrates at active seep sites in the eastern Black Sea using pressure coring
24 technique. *Biogeosciences* 8, 3555–3565. <https://doi.org/10.5194/bg-8-3555-2011>
- 25 Jørgensen, B.B., Böttcher, M.E., Lüschen, H., Neretin, L.N., Volkov, I.I., 2004. Anaerobic
26 methane oxidation and a deep H₂S sink generate isotopically heavy sulfides in Black Sea
27 sediments. *Geochim. Cosmochim. Acta* 68, 2095–2118.
28 <https://doi.org/10.1016/j.gca.2003.07.017>
- 29 Kennett, J., Hendy, I., Bebout, G., Friedrichs, C., Horwitz, L., Levin, L., Lyons, W., Strobel,
30 D., Young, W., Kennett, I., James, P., 2003. Methane Hydrates in the Clathrate Gun
31 Hypothesis. *AGU Monogr.* ed. Washington, DC.
- 32 Ker, S., Thomas, Y., Riboulot, V., Sultan, N., Bernard, C., Scalabrin, C., Ion, G., Marsset, B.,
33 2019. Anomalously Deep BSR Related to a Transient State of the Gas Hydrate System in
34 the Western Black Sea. *Geochemistry, Geophys. Geosystems* 20, 442–459.
35 <https://doi.org/10.1029/2018GC007861>
- 36 Khlystov, O., Batist, M. De, Shoji, H., Hachikubo, A., Nishio, S., Naudts, L., Poort, J.,
37 Khabuev, A., Belousov, O., Manakov, A., Kalmychkov, G., 2013. Gas hydrate of Lake
38 Baikal: Discovery and varieties. *J. Asian Earth Sci.* 62, 162–166.
39 <https://doi.org/10.1016/j.jseaes.2012.03.009>
- 40 Kida, M., Hachikubo, A., Sakagami, H., Minami, H., Krylov, A., Yamashita, S., Takahashi,
41 N., Shoji, H., Khlystov, O., Poort, J., Narita, H., 2009. Natural gas hydrates with locally
42 different cage occupancies and hydration numbers in Lake Baikal. *Geochemistry,*

- 1 Geophys. Geosystems 10, 1–8. <https://doi.org/10.1029/2009GC002473>
- 2 Kida, M., Khlystov, O., Zemskaya, T., Takahashi, N., Minami, H., Sakagami, H., Krylov, A.,
3 Hachikubo, A., Yamashita, S., Shoji, H., Poort, J., Naudts, L., 2006. Coexistence of
4 structure I and II gas hydrates in Lake Baikal suggesting gas sources from microbial and
5 thermogenic origin. *Geophys. Res. Lett.* 33, 10–13.
6 <https://doi.org/10.1029/2006GL028296>
- 7 Klapp, S.A., Murshed, M.M., Pape, T., Klein, H., Bohrmann, G., Brewer, P.G., Kuhs, W.F.,
8 2010. Mixed gas hydrate structures at the Chapopote Knoll, southern Gulf of Mexico.
9 *Earth Planet. Sci. Lett.* 299, 207–217. <https://doi.org/10.1016/j.epsl.2010.09.001>
- 10 Kuhs, W.F., Genov, G., Staykova, D.K., Hansen, T., 2004. Ice perfection and onset of
11 anomalous preservation of gas hydrates. *Phys. Chem. Chem. Phys.* 6, 4917–4920.
12 <https://doi.org/10.1039/B412866D>
- 13 Kumar, P., Das, H.C., Anbazhagan, K., Lu, H., Ripmeester, J. a, 2008. Structural
14 Characterization of Natural Gas Hydrates. *Proc. 6th Int. Conf. Gas Hydrates (ICGH*
15 *2008)*. <https://doi.org/10.1039/B412866D>
- 16 Kvenvolden, K.A., 1988. Methane hydrate - A major reservoir of carbon in the shallow
17 geosphere? *Chem. Geol.* 71, 41–51. [https://doi.org/10.1016/0009-2541\(88\)90104-0](https://doi.org/10.1016/0009-2541(88)90104-0)
- 18 Kvenvolden, K.A., 1998. A primer on the geological occurrence of gas hydrate service
19 Permission Subscribe. *Geol. Soc. London, Spec. Publ.* 137, 9–30.
20 <https://doi.org/10.1144/GSL.SP.1998.137.01.02>
- 21 Liu, C., Meng, Q., He, X., Li, C., Ye, Y., Zhang, G., Liang, J., 2015. Characterization of
22 natural gas hydrate recovered from Pearl River Mouth basin in South China Sea. *Mar.*
23 *Pet. Geol.* 61, 14–21. <https://doi.org/10.1016/j.marpetgeo.2014.11.006>
- 24 Liu, C., Ye, Y., Meng, Q., He, X., Lu, H., Zhang, J., Liu, J., Yang, S., 2012. The
25 Characteristics of Gas Hydrates Recovered from Shenhu Area in the South China Sea.
26 *Mar. Geol.* 307–310, 22–27. <https://doi.org/10.1016/j.margeo.2012.03.004>
- 27 Lu, H., Kawasaki, T., Ukita, T., Moudrakovski, I., Fujii, T., Noguchi, S., Shimada, T.,
28 Nakamizu, M., Ripmeester, J., Ratcliffe, C., 2011a. Particle size effect on the saturation
29 of methane hydrate in sediments – Constrained from experimental results. *Mar. Pet.*
30 *Geol.* 28, 1801–1805. <https://doi.org/10.1016/j.marpetgeo.2010.11.007>
- 31 Lu, H., Lorenson, T.D., Moudrakovski, I.L., Ripmeester, J.A., Collett, T.S., Hunter, R.B.,
32 Ratcliffe, C.I., 2011b. The characteristics of gas hydrates recovered from the Mount
33 Elbert Gas Hydrate Stratigraphic Test Well, Alaska North Slope. *Mar. Pet. Geol.* 28,
34 411–418. <https://doi.org/10.1016/j.marpetgeo.2010.01.002>
- 35 Lu, H., Moudrakovski, I., Riedel, M., Spence, G., Dutrisac, R., Ripmeester, J., Wright, F.,
36 Dallimore, S., 2005. Occurrence and structural characterization of gas hydrates
37 associated with a cold vent field, offshore Vancouver Island. *J. Geophys. Res.* 110,
38 B10204. <https://doi.org/10.1029/2005JB003900>
- 39 Lu, H., Seo, Y., Lee, J., Moudrakovski, I., Ripmeester, J.A., Chapman, N.R., Coffin, R.B.,
40 Gardner, G., Pohlman, J., 2007. Complex gas hydrate from the Cascadia margin. *Nature*
41 445, 303–306. <https://doi.org/10.1038/nature05463>

- 1 Lu, S.-M., 2015. A global survey of gas hydrate development and reserves: Specifically in the
2 marine field. *Renew. Sustain. Energy Rev.* 41, 884–900.
3 <https://doi.org/10.1016/j.rser.2014.08.063>
- 4 Lu, Z., Zhu, Y., Zhang, Y., Wen, H., Li, Y., Liu, C., 2011. Gas hydrate occurrences in the
5 Qilian Mountain permafrost, Qinghai Province, China. *Cold Reg. Sci. Technol.* 66, 93–
6 104. <https://doi.org/10.1016/j.coldregions.2011.01.008>
- 7 Machel, H., 2001. Bacterial and thermochemical sulfate reduction in diagenetic settings —
8 old and new insights. *Sediment. Geol.* 140, 143–175. [https://doi.org/10.1016/S0037-
9 0738\(00\)00176-7](https://doi.org/10.1016/S0037-0738(00)00176-7)
- 10 Machel, H., Krouse, H., Sassen, R., 1995. Products and distinguishing criteria of bacterial and
11 thermochemical sulfate reduction. *Appl. Geochemistry* 10, 373–389.
12 [https://doi.org/10.1016/0883-2927\(95\)00008-8](https://doi.org/10.1016/0883-2927(95)00008-8)
- 13 Makogon, Y.F., Holditch, S.A., Makogon, T.Y., 2007. Natural gas-hydrates — A potential
14 energy source for the 21st Century. *J. Pet. Sci. Eng.* 56, 14–31.
15 <https://doi.org/10.1016/j.petrol.2005.10.009>
- 16 Manheim, F., Chan, K., 1974. Interstitial Waters of Black Sea Sediments: New Data and
17 Review, in: *The Black Sea - Geology, Chemistry and Biology*. pp. 155–180.
18 <https://doi.org/10.1306/M20377C45>
- 19 Maslin, M., Owen, M., Betts, R., Day, S., Dunkley Jones, T., Ridgwell, A., 2010. Gas
20 hydrates: past and future geohazard? *Philos. Trans. R. Soc. A Math. Phys. Eng. Sci.* 368,
21 2369–2393. <https://doi.org/10.1098/rsta.2010.0065>
- 22 Milkov, A. V., Etiope, G., 2018. Revised genetic diagrams for natural gases based on a global
23 dataset of >20,000 samples. *Org. Geochem.* 125, 109–120.
24 <https://doi.org/10.1016/j.orggeochem.2018.09.002>
- 25 Milkov, A. V., 2011. Organic Geochemistry Worldwide distribution and significance of
26 secondary microbial methane formed during petroleum biodegradation in conventional
27 reservoirs. *Org. Geochem.* 42, 184–207.
28 <https://doi.org/10.1016/j.orggeochem.2010.12.003>
- 29 Minshull, T.A., Marín-Moreno, H., Betlem, P., Bialas, J., Bünz, S., Burwicz, E., Cameselle,
30 A.L., Cifci, G., Giustiniani, M., Hillman, J.I.T., Hölz, S., Hopper, J.R., Ion, G., León, R.,
31 Magalhaes, V., Makovsky, Y., Mata, M.-P., Max, M.D., Nielsen, T., Okay, S.,
32 Ostrovsky, I., O'Neill, N., Pinheiro, L.M., Plaza-Faverola, A.A., Rey, D., Roy, S.,
33 Schwalenberg, K., Senger, K., Vadakkepuliymbatta, S., Vasilev, A., Vázquez, J.-T.,
34 2020. Hydrate occurrence in Europe: A review of available evidence. *Mar. Pet. Geol.*
35 111, 735–764. <https://doi.org/10.1016/j.marpetgeo.2019.08.014>
- 36 Moryama, C.T., Sugahara, T., Yatabe Franco, D.Y., Mimachi, H., 2015. In Situ Raman
37 Spectroscopic Studies on Small-Cage Occupancy of Methane in the Simple Methane and
38 Methane + Deuterated Tetrahydrofuran Mixed Hydrates. *J. Chem. Eng. Data* 60, 3581–
39 3587. <https://doi.org/10.1021/acs.jced.5b00533>
- 40 Nasif, A., Özel, F.E., Dondurur, D., 2020. Seismic identification of gas hydrates: A case study
41 from Sakarya Canyon, western Black Sea. *Turkish J. Earth Sci.* 29, 434–454.
42 <https://doi.org/10.3906/yer-1909-2>

- 1 Naudts, L., Greinert, J., Artemov, Y., Staelens, P., Poort, J., Van Rensbergen, P., De Batist,
2 M., 2006. Geological and morphological setting of 2778 methane seeps in the Dnepr
3 paleo-delta, northwestern Black Sea. *Mar. Geol.* 227, 177–199.
4 <https://doi.org/10.1016/j.margeo.2005.10.005>
- 5 Pape, T., Bahr, A., Klapp, S.A., Abegg, F., Bohrmann, G., 2011. High-intensity gas seepage
6 causes rafting of shallow gas hydrates in the southeastern Black Sea. *Earth Planet. Sci.*
7 *Lett.* 307, 35–46. <https://doi.org/10.1016/j.epsl.2011.04.030>
- 8 Pape, T., Bahr, A., Rethemeyer, J., Kessler, J.D., Sahling, H., Hinrichs, K.-U., Klapp, S.A.,
9 Reeburgh, W.S., Bohrmann, G., 2010. Molecular and isotopic partitioning of low-
10 molecular-weight hydrocarbons during migration and gas hydrate precipitation in
11 deposits of a high-flux seepage site. *Chem. Geol.* 269, 350–363.
12 <https://doi.org/10.1016/j.chemgeo.2009.10.009>
- 13 Pape, T., Haeckel, M., Riedel, M., Kölling, M., Schmidt, M., Wallmann, K., Bohrmann, G.,
14 2020. Formation pathways of light hydrocarbons in deep sediments of the Danube deep-
15 sea fan, Western Black Sea. *Mar. Pet. Geol.* 122, 104627.
16 <https://doi.org/10.1016/j.marpetgeo.2020.104627>
- 17 Parker, S.F., Tavender, S.M., Dixon, N.M., Herman, H., Williams, K.P.J., Maddams, W.F.,
18 1999. Raman Spectrum of β -Carotene Using Laser Lines from Green (514.5 nm) to
19 Near-Infrared (1064 nm): Implications for the Characterization of Conjugated Polyenes.
20 *Appl. Spectrosc.* 53, 86–91. <https://doi.org/10.1366/0003702991945263>
- 21 Paull, C.K., Dillon, W.P., 2000. Natural Gas Hydrates: occurrence, distribution and detection.
22 AGU Monographs, Washington DC.
- 23 Popescu, I., Lericolais, G., Panin, N., De Batist, M., Gillet, H., 2007. Seismic expression of
24 gas and gas hydrates across the western Black Sea. *Geo-Marine Lett.* 27, 173–183.
25 <https://doi.org/10.1007/s00367-007-0068-0>
- 26 Qin, J., Kuhs, W.F., 2013. Quantitative Analysis of Gas Hydrates Using Raman
27 Spectroscopy. *Am. Inst. Chem. Eng.* 1–13. <https://doi.org/10.1002/aic.13994>
- 28 Qin, J., Kuhs, W.F., 2015. Calibration of Raman Quantification Factors of Guest Molecules in
29 Gas Hydrates and Their Application to Gas Exchange Processes Involving N₂. *J. Chem.*
30 *Eng. Data* 60, 369–375. <https://doi.org/https://doi.org/10.1021/je500613y>
- 31 Reeburgh, W., 1976. Methane consumption in cariaco trench waters and sediments. *Earth*
32 *Planet. Sci. Lett.* 28, 337–344. [https://doi.org/10.1016/0012-821X\(76\)90195-3](https://doi.org/10.1016/0012-821X(76)90195-3)
- 33 Reitz, A., Pape, T., Haeckel, M., Schmidt, M., Berner, U., Scholz, F., Liebetrau, V., Aloisi,
34 G., Weise, S.M., Wallmann, K., 2011. Sources of fluids and gases expelled at cold seeps
35 offshore Georgia, eastern Black Sea. *Geochim. Cosmochim. Acta* 75, 3250–3268.
36 <https://doi.org/10.1016/j.gca.2011.03.018>
- 37 Riboulot, V., Cattaneo, A., Scalabrin, C., Gaillot, A., Jouet, G., Ballas, G., Marsset, T.,
38 Garziglia, S., Ker, S., 2017. Control of the geomorphology and gas hydrate extent on
39 widespread gas emissions offshore Romania. *Bull. Soc. Géol. Fr.* 188, 1–12.
40 <https://doi.org/10.1051/bsgf/2017182>
- 41 Riboulot, V., Ker, S., Sultan, N., Thomas, Y., Marsset, B., Scalabrin, C., Ruffine, L., Boulart,
42 C., Ion, G., 2018. Freshwater lake to salt-water sea causing widespread hydrate

- 1 dissociation in the Black Sea. *Nat. Commun.* 9, 1–8. [https://doi.org/10.1038/s41467-017-](https://doi.org/10.1038/s41467-017-02271-z)
2 02271-z
- 3 Ripmeester, J., Lu, H., Moudrakovski, I., Dutrisac, R., Wilson, L., Wright, F., Dallimore, S.,
4 2005. Structure and composition of hydrate in sediment recovered from Mallik 5L-38,
5 Mackenzie Delta, NWT Canada: X-ray diffraction, Raman and Solid-state NMR
6 spectroscopy. *Geol. Surv. Canada* 585, 1–6. <https://doi.org/10.4095/220702>
- 7 Römer, M., Sahling, H., Pape, T., Bahr, A., Feseker, T., Wintersteller, P., Bohrmann, G.,
8 2012. Geological control and magnitude of methane ebullition from a high-flux seep area
9 in the Black Sea—the Kerch seep area. *Mar. Geol.* 319–322, 57–74.
10 <https://doi.org/10.1016/j.margeo.2012.07.005>
- 11 Ross, D., Degens, E., 1974. Recent Sediments of Black Sea, in: *The Black Sea - Geology,*
12 *Chemistry, and Biology.* American Association of Petroleum Geologists.
13 <https://doi.org/10.1306/M20377>
- 14 Ruffine, L., Deusner, C., Haeckel, M., Kossel, E., Toucanne, S., Chéron, S., Boissier, A.,
15 Schmidt, M., Donval, J.-P., Scholz, F., Guyader, V., Ker, S., Riboulot, V., 2021. Effects
16 of postglacial seawater intrusion on sediment geochemical characteristics in the
17 Romanian sector of the Black Sea. *Mar. Pet. Geol.* 123, 104746.
18 <https://doi.org/10.1016/j.marpetgeo.2020.104746>
- 19 Ruffine, L., Donval, J.-P., Croguennec, C., Burnard, P., Lu, H., Germain, Y., Legoix, L.N.,
20 Bignon, L., Çağatay, M.N., Marty, B., Madre, D., Pitel-Roudaut, M., Henry, P., Géli, L.,
21 2018. Multiple gas reservoirs are responsible for the gas emissions along the Marmara
22 fault network. *Deep Sea Res. Part II Top. Stud. Oceanogr.* 153, 48–60.
23 <https://doi.org/10.1016/j.dsr2.2017.11.011>
- 24 Ruppel, C.D., Kessler, J.D., 2017. The interaction of climate change and methane hydrates.
25 *Rev. Geophys.* 55, 126–168. <https://doi.org/10.1002/2016RG000534>
- 26 Rusakov, O., Kutas, R., 2018. Mantle origin of methane in the Black Sea. *Geofiz. Zhurnal* 40,
27 191–207. <https://doi.org/10.24028/gzh.0203-3100.v40i5.2018.147482>
- 28 Salamatin, A.N., Falenty, A., Kuhs, W.F., 2017. Diffusion Model for Gas Replacement in an
29 Isostructural CH₄-CO₂ Hydrate System. *J. Phys. Chem. C* 121, 17603–17616.
30 <https://doi.org/10.1021/acs.jpcc.7b04391>
- 31 Schicks, J.M., Ziemann, M.A., Lu, H., Ripmeester, J.A., 2010. Raman spectroscopic
32 investigations on natural samples from the Integrated Ocean Drilling Program (IODP)
33 Expedition 311: Indications for heterogeneous compositions in hydrate crystals.
34 *Spectrochim. Acta - Part A Mol. Biomol. Spectrosc.* 77, 973–977.
35 <https://doi.org/10.1016/j.saa.2010.08.033>
- 36 Schmale, O., Greinert, J., Rehder, G., 2005. Methane emission from high-intensity marine gas
37 seeps in the Black Sea into the atmosphere. *Geophys. Res. Lett.* 32, 1–4.
38 <https://doi.org/10.1029/2004GL021138>
- 39 Schmale, O., Haeckel, M., McGinnis, D.F., 2011. Response of the Black Sea methane budget
40 to massive short-term submarine inputs of methane. *Biogeosciences* 8, 911–918.
41 <https://doi.org/10.5194/bg-8-911-2011>
- 42 Seo, Y., Kang, S.P., Jang, W., 2009. Structure and Composition Analysis of Natural Gas

- 1 Hydrates: ^{13}C NMR spectroscopic and gas uptake measurements of mixed gas hydrates.
2 *J. Phys. Chem. A* 113, 9641–9649. <https://doi.org/10.1021/jp904994s>
- 3 Shin, D., Cha, M., Yang, Y., Choi, S., Woo, Y., Lee, J.W., Ahn, D., Im, J., Lee, Y., Han,
4 O.H., Yoon, J.H., 2017. Temperature- and pressure-dependent structural transformation
5 of methane hydrates in salt environments. *Geophys. Res. Lett.* 44, 2129–2137.
6 <https://doi.org/10.1002/2016GL072277>
- 7 Sloan, E., Koh, C., 2008. *Clathrate Hydrates of Natural Gases*. CRC Press, New York.
- 8 Song, Y., Yang, L., Zhao, J., Liu, W., Yang, M., Li, Y., Liu, Y., Li, Q., 2014. The status of
9 natural gas hydrate research in China : A review. *Renew. Sustain. Energy Rev.* 31, 778–
10 791. <https://doi.org/10.1016/j.rser.2013.12.025>
- 11 Soulet, G., Delaygue, G., Vallet-Coulomb, C., Böttcher, M.E., Sonzogni, C., Lericolais, G.,
12 Bard, E., 2010. Glacial hydrologic conditions in the Black Sea reconstructed using
13 geochemical pore water profiles. *Earth Planet. Sci. Lett.* 296, 57–66.
14 <https://doi.org/10.1016/j.epsl.2010.04.045>
- 15 Soulet, G., Ménot, G., Lericolais, G., Bard, E., 2011. A revised calendar age for the last
16 reconnection of the Black Sea to the global ocean. *Quat. Sci. Rev.* 30, 1019–1026.
17 <https://doi.org/10.1016/j.quascirev.2011.03.001>
- 18 Sum, A.K., Burruss, R.C., Sloan, E.D., 1997. Measurement of Clathrate Hydrates via Raman
19 Spectroscopy. *J. Phys. Chem.* 101, 7371–7377. <https://doi.org/10.1021/jp970768e>
- 20 Uchida, T., Hirano, T., Ebinuma, T., Narita, H., Gohara, K., Mae, S., Matsumoto, R., 1999.
21 Raman Spectroscopic Determination of Hydration Number of Methane Hydrates. *Am.*
22 *Inst. Chem. Eng.* 45, 2641–2645. <https://doi.org/10.1002/aic.690451220>
- 23 Urmos, J., Sharma, S.K., Mackenzie, F.T., 1991. Characterization of some biogenic
24 carbonates with Raman spectroscopy. *Am. Mineral.* 76, 641–646.
- 25 van Cleef, A., Diepen, G.A., 1965. Gas hydrates of nitrogen and oxygen. II. *Recl. des Trav.*
26 *Chim. des Pays-Bas* 84, 1085–1093.
- 27 van der Waals, J.H., Platteeuw, J.C., 1958. Clathrate solutions, in: I. Progonine (Ed.),
28 *Advance in Chemical Physics*. John Wiley & Sons, Inc., pp. 1–57.
- 29 Wallmann, K., Pinerro, E., Burwicz, E., Haeckel, M., Hensen, C., Dale, A., Ruepke, L., 2012.
30 The Global Inventory of Methane Hydrate in Marine Sediments: A Theoretical
31 Approach. *Energies* 5, 2449–2498. <https://doi.org/10.3390/en5072449>
- 32 Wang, F., Zhao, B., Li, G., 2018. Prevention of Potential Hazards Associated with Marine
33 Gas Hydrate Exploitation: A Review. *Energies* 11, 2384.
34 <https://doi.org/10.3390/en11092384>
- 35 Withnall, R., Chowdhry, B.Z., Silver, J., Edwards, H.G.M., de Oliveira, L.F.C., 2003. Raman
36 spectra of carotenoids in natural products. *Spectrochim. Acta Part A Mol. Biomol.*
37 *Spectrosc.* 59, 2207–2212. [https://doi.org/10.1016/S1386-1425\(03\)00064-7](https://doi.org/10.1016/S1386-1425(03)00064-7)
- 38 Yang, L., Qin, J., Kuhs, W.F., 2019. Personal communication.
- 39 Yeon, S., Seol, J., Koh, D., Seo, Y., Park, K., Huh, D., Lee, J., Lee, H., 2011. Abnormal

- 1 methane occupancy of natural gas hydrates in deep sea floor sediments. *Energy Environ.*
2 *Sci.* 4, 421–424. <https://doi.org/10.1039/C0EE00355G>
- 3 Yeon, S., Seol, J., Seo, Y., Park, Y., Koh, D., Park, K., Huh, D., Lee, J., Lee, H., 2009. Effect
4 of Interlayer Ions on Methane Hydrate Formation in Clay Sediments. *J. Phys. Chem. B*
5 113, 1245–1248. <https://doi.org/10.1021/jp810079c>
- 6 Yousuf, M., Qadri, S.B., Knies, D.L., Grabowski, K.S., Coffin, R.B., Pohlman, J.W., 2004.
7 Novel results on structural investigations of natural minerals of clathrate hydrates. *Appl.*
8 *Phys. A* 78, 925–939. <https://doi.org/10.1007/s00339-003-2091-y>
- 9 Zander, T., Haeckel, M., Klaucke, I., Bialas, J., Klaeschen, D., Papenberg, C., Pape, T.,
10 Berndt, C., Bohrmann, G., 2020. New insights into geology and geochemistry of the
11 Kerch seep area in the Black Sea. *Mar. Pet. Geol.* 113, 104162.
12 <https://doi.org/10.1016/j.marpetgeo.2019.104162>
- 13 Zhang, X., Du, Z., Zheng, R., Luan, Z., Qi, F., Cheng, K., Wang, B., Ye, W., Liu, X., Lian,
14 C., Chen, C., Guo, J., Li, Y., Yan, J., 2017. Development of a new deep-sea hybrid
15 Raman insertion probe and its application to the geochemistry of hydrothermal vent and
16 cold seep fluids. *Deep. Res. Part I* 123, 1–12. <https://doi.org/10.1016/j.dsr.2017.02.005>
- 17 Zhang, X., Walz, P.M., Kirkwood, W.J., Hester, K.C., Ussler, W., Peltzer, E.T., Brewer, P.G.,
18 2010. Development and deployment of a deep-sea Raman probe for measurement of
19 pore water geochemistry. *Deep. Res. Part I* 57, 297–306.
20 <https://doi.org/10.1016/j.dsr.2009.11.004>

21

HIGHLIGHTS

- NGH from Black Sea are investigated by gas chromatography and Raman spectroscopy
- The hydrates are structure SI and contain mainly CH₄ and small amounts of N₂ and CO₂
- CH₄ being generated by the reduction of CO₂
- 2D-Raman reveals spatial variability in guests' distribution and hydrate composition
- Raman imaging analysis shows a spatial variability of the cage occupancy

Journal Pre-proof

Declaration of interests

The authors declare that they have no known competing financial interests or personal relationships that could have appeared to influence the work reported in this paper.

The authors declare the following financial interests/personal relationships which may be considered as potential competing interests:

Journal Pre-proof